EFDA–JET–PR(13)57

S. Moradi, I. Pusztai, I. Voitsekhovitch, L. Garzotti, C. Bourdelle,
M.J. Pueschel, I. Lupelli, M. Romanelli and JET EFDA contributors*

Core Micro-Instability Analysis of JET Hybrid and Baseline Discharges with Carbon Wall

Core Micro-Instability Analysis of JET Hybrid and Baseline Discharges with Carbon Wall

S. Moradi[1,2], I. Pusztai[2,3], I. Voitsekhovitch[4], L. Garzotti[4], C. Bourdelle[5], M.J. Pueschel[6], I. Lupelli[4], M. Romanelli[4] and JET EFDA contributors*

JET-EFDA, Culham Science Centre, OX14 3DB, Abingdon, UK

[1]Ecole Polytechnique, CNRS UMR7648, LPP, F-91128, Palaiseau, France
[2]Applied Physics, Chalmers University of Technology, Göteborg 41296, Sweden
[3]Plasma Science and Fusion Center, Massachusetts Institute of Technology, Cambridge MA, 02139, USA
[4]JET-EFDA, Culham Science Centre, Abingdon, OX14 3DB, UK
[5]IRFM, CEA, F-13108 Saint Paul-Lez-Durance, France
[6]University of Wisconsin-Madison, Madison, Wisconsin 53706, USA
** See annex of F. Romanelli et al, "Overview of JET Results", (24th IAEA Fusion Energy Conference, San Diego, USA (2012)).*

Preprint of Paper to be submitted for publication in
Nuclear Fusion

ABSTRACT

The core micro-instability characteristics of hybrid and baseline plasmas in a selected set of JET plasmas with carbon wall are investigated through local linear and non-linear gyrokinetic simulations with the GYRO code [J. Candy and E. Belli, General Atomics Report GA-A26818 (2011)]. In particular, we study the role of plasma pressure on the microinstabilities, and scan the parameter space for the important plasma parameters responsible for the onset and stabilization of the modes under experimental conditions. We find that a good core confinement due to strong stabilization of the micro-turbulence driven transport can be expected in the hybrid plasmas due to the stabilizing effect of the fast ion pressure that is more effective at the low magnetic shear of the hybrid discharges. While parallel velocity gradient destabilization is important for the inner core, at outer radii the hybrid plasmas may benefit from a strong quench of the turbulence transport by **E×B** rotation shear. abstract

1. INTRODUCTION

In recent years there has been an increasing worldwide effort in the development of the so-called hybrid or improved H-mode scenarios as a hybrid between an AT and a baseline plasma [2–5]. In these scenarios, by optimizing the current density profile, an enhanced normalized confinement can be achieved, as compared to the ITER baseline scenario, the ELMy H-mode.

Also, a higher bootstrap fraction and a lower requirement for induced current allows longer pulses in the hybrid mode. A limiting factor for the plasma performance and achievable normalized plasma pressure β_N(= $\bar{\beta}a$[m] B_T[T] / I_P [MA], with $\bar{\beta}$, the volume averaged normalized pressure, a the plasma minor radius, B_T the toroidal magnetic field and IP the plasma current), is the onset of core MHD activity such as m/n = 2 / 1, 3 / 2 neoclassical tearing modes [6]. However, by tailoring the current profile the destabilization of these large MHD activities can be avoided by slowing down the current diffusion time and hence prolonging the time period when the safety-factor profile is flat but kept above 1 ($q_0 > 1$) and a radially extended low magnetic shear region is present in the plasma core. These developments gave rise to the so-called hybrid or improved H-mode scenarios [5].

The method used at Joint European Torus (JET) for slowing down the current diffusion in the hybrid scenarios is through an overshoot of the current in the pre-heating phase just before reducing it to its flat-top value during the main heating phase [7–9]. This method allows for the broadening of the current profile with flat core q-profile over a large part of plasma radius which results in an enhancement of the confinement factor H_{98}(y, 2) compared to what could be obtained with a regular ramp-up scenario (baseline scenario). For the definition of H_{98}(y, 2) see Ref. [10] and references therein.

During the 2008-2009 experimental campaigns at the JET, a remarkable improvement in the normalized confinement was achieved in hybrid scenarios (H_{98}(y, 2) ~ 1.3–1.4) in both high ($\delta = 0.4$) and low ($\delta = 0.2$) triangularity plasmas [8, 11]. The plasma configurations are optimized to reduce the wall interactions and therefore the recycling of the wall neutrals. In the hybrid plasmas lower density and higher temperature are achieved.

In a recent work, Ref. [11], the confinement properties of the hybrid and baseline plasmas in a database of 112 discharges in JET with Carbon Fiber Composite (CFC) wall have been analyzed. Here, it has been shown that the confinement factor $H_{98}(y, 2)$ in JET hybrid plasmas are typically $1 < H_{98}(y, 2) < 1.5$ while in the baseline ELMy H-mode plasmas typical values are $H_{98}(y, 2) \sim 1$. However, the underlying physics basis for the observed increased normalized confinement remain somewhat unclear, making the hybrid plasmas an interesting choice for modeling and trying to explain the underlying mechanisms responsible for their deviation from the "known" H-mode confinement. Moreover, due to their high normalized pressure, electromagnetic effects and their impact on the turbulent transport driven by micro-instabilities has to be investigated.

Recent reports have shown the significant role of electromagnetic modes such as Micro- Tearing Modes (MTMs) and Kinetic-Ballooning Modes (KBMs) on the heat and particle transport in the core of fusion plasmas [12–18]. In the presence of high β ($= 8\pi \langle p \rangle / B^2_T$, with $\langle p \rangle$ being the volume average kinetic pressure), it has been shown that the electrostatic modes such as Ion Temperature Gradient Modes (ITG) may be fully stabilized while electromagnetic modes are destabilized as β is increased and therefore can give rise to a new regime with high turbulent transport. However, since in the hybrid plasmas the confinement shows improvement despite the increased β it is important to understand the possible stabilization mechanisms for the electromagnetic modes which are at play in these plasmas. Furthermore, the impact of plasma shape on electromagnetic modes is shown to be stronger than on electrostatic modes [12–14]. Therefore, it is important to include plasma shaping when studying these modes.

In this paper therefore, we investigate the characteristics of core micro-instabilities in two hybrid and two baseline plasmas in JET selected from the database analyzed in Ref. [11] through local linear and non-linear gyro-kinetic simulations using the GYRO code [19, 20]. In particular, we study the role of plasma pressure micro-instabilities, and scan the parameter space for the important plasma parameters responsible for the onset and stabilization of the modes under realistic conditions.

The remainder of the paper is organized as follows. In Sec.5 we discuss the studied discharges, the data analysis, and the set of input parameters used in the simulations. In Sec.3 we present the gyrokinetic microinstability analysis of the chosen scenarios. To assess the sensitivity of the results and to identify possible stabilizing mechanisms, we perform scans in plasma profile and geometry parameters around their nominal values with special emphasis on finite-β, plasma shaping, and fast ion effects. Finally, we discuss or results and conclude in Sec.5.

2. EXPERIMENTAL DATA USED IN SIMULATIONS

Four JET discharges are chosen for our study: two hybrid discharges: Pulse No's: 77922 and 75225 with high and low triangularity respectively, and two baseline discharges: Pulse No's: 76679 and 78682, again with high and low triangularity respectively. These discharges have been chosen from the database presented in Ref.[11] as part of the 2008-2009 JET experimental campaigns with CFC wall. More detailed descriptions of the experimental set up in these discharges can be found in Refs. [9, 11]. Here, we would like to note that these shots are arbitrary selected examples of hybrid and

baseline plasmas, and they are not specifically chosen similarity discharges. As a consequence, the conclusions drawn for these discharges might not be general and may not extrapolate to the whole group of hybrid and baseline H-mode discharges.

Figure 1 shows the profiles of electron plasma density n_e, ion and electron temperatures $T_{i,e}$, toroidal rotation speed V_{tor} (for the baseline, only in the high-δ case) measured at outboard mid-plane and re-mapped on TRANSP [21] equilibrium, and safety factor q for the selected discharges. In hybrid discharges the q-profiles have been reconstructed in the EFIT simulations constrained by Motional Stark Effect (MSE) measurements [9, 22]. In baseline discharges the q-profiles have been simulated by TRANSP using NCLASS module for current conductivity and bootstrap current. The q-profile at the beginning of NBI heating phase reconstructed with EFIT constrained by magnetic probe measurements has been used as an initial condition for current diffusion simulations. However, the calculated q in the core may be too low in these cases.

The plasma profiles shown in Fig.1 are averaged over a time window of 0.5s over the period of the highest $H_{98}(y, 2)$ factor with nearly stationary temperatures and density. The hybrid plasmas do not show any Neoclassical Tearing Mode (NTM) activity during the selected time window, while in baseline plasmas a n = 1 mode is present. Figure 2 illustrates time traces of the plasma parameters: total input NBI power P_{tot}, plasma current I_P, normalized thermal pressure, the global confinement enhancement factor $H_{98}(y, 2)$ and the Greenwald density fraction $F_{GDL} \sim \bar{n}/n_{gw}$ are shown (where $\bar{n}$ is the line averaged density, and $n_{gw}[m^{-3}] = 10^{20} I_p [MA] / \pi a[m]^2$ with a being the minor radius) and the highlighted bars denote the time period over which the profiles were averaged. The characteristics of the hybrid scenarios with the current overshoot in the preheating phase as compared to baseline regular ramp-up scenarios can be seen on the time traces of the plasma current in Fig. 2(b). Also, note that hybrids operate at lower plasma currents than baselines.

As seen in Fig.1(a), plasma density in hybrid plasmas is lower compared to those of the baselines as a result of lower current. The fueling level for the baseline discharges is: $\Gamma_{D2} \sim 0.4–4\times10^{22}$ electron s^{-1}, whereas for the hybrid plasmas the fueling is generally low, with $\Gamma_{D2} \sim 0–0.25\times10^{22}$ electron s^{-1}. In the hybrid plasmas it is difficult to increase the density by higher gas fueling as it can result in degradation of pedestal confinement, leading to a reduction of density. The fuelling waveforms for the two selected hybrid discharges can be found in Ref.[11] figure 4).

The input powers were also different between hybrid ($P_{tot} \sim 17–20$MW) and baseline plasmas ($P_{tot} \sim 10–13$MW), leading to the higher temperatures and toroidal rotation in hybrids as seen in Fig.1(b,d) and (e). No ICRH heating is applied in these hybrid plasmas, but to avoid impurity accumulation a small amount of central ICRH heating ($P_{ICRH} < 10\% P_{NBI}$) has been applied in baseline plasmas [11]. As shown in Fig.1(c) the safety factor in hybrid discharges has a broader flat region in the core and it is higher at the edge, as compared to the baseline discharges.

For our core micro-instability analysis two radial positions are chosen: $r/a = 0.3$ and 0.6, where r is the half-width of the flux surfaces, and a is r at the separatrix (as defined in [20]). Using the profiles shown in Fig.1, tables I-IV present the local plasma parameters used in our study for each of the four selected discharges at the two radial positions. Magnetic geometry parameters, such as

those describing the shaping of flux surfaces or the q-profile, can be changed independently in the GYRO code, see Refs.[23, 24]. Here in the hybrid cases these parameters are based on magnetic geometries from EFIT constrained by MSE measurements, whereas in baselines are simulated by TRANSP using NCLASS module for current conductivity and bootstrap current. The density and temperature scale lengths are defined as: $L_n = -[\partial(\ln n)/\partial \mathrm{r}]^{-1}$, $L_T = -[\partial(\ln T)/\partial \mathrm{r}]^{-1}$. The safety factor is $q = d\chi_t/d\psi$, with $2\pi\chi_t$ is the toroidal flux, and $2\pi\psi$ being the poloidal flux, and the magnetic shear is $s = (r/q)dq/dr$. In these tables, β_e is calculated following the expression:

$$\beta_e = \frac{8\pi(n_e[10^{19}/m^3]\ 10^{-6}\ 10^{19})(T_e[keV]\ 1.6022\ 10^{-9})}{(10^4\ B_{unit}\ [T])^2}, \tag{1}$$

where B_{unit} is defined as the effective field strength, see Refs. [23, 25],

$$B_{unit} = \frac{1}{r}\frac{d\chi_t}{dr}. \tag{2}$$

Note that for a plasma with T_e/T_i, we have $\beta = 2\beta_e$.

Furthermore, $\in$ is the inverse aspect ratio, κ is the elongation, δ is the triangularity, and $s_\delta = \mathrm{r}\partial\delta/\partial\mathrm{r}$, and $s_\kappa = (\mathrm{r}/\kappa)\partial\kappa/\partial\mathrm{r}$ are the triangularity and elevation shear, respectively. The convention of defining β_e in terms of B_{unit} is specific to GYRO, and not to gyrokinetic codes in general. We note that B_{unit} in shaped plasmas is not equal to the on-axis magnetic field B, because the effective radius r is defined as the half width of the flux surface at the elevation of its centroid and thus the toroidal flux inside a given flux surface is generally not equal to $\mathrm{r}^2\pi\bar{B}$. Since for elongated flux surfaces ($\kappa > 1$) the area of the cross section of the flux surface is larger than πr^2, the effective field is roughly times larger than the on-axis field. It is important that it is β_e, defined with the *effective field*, that matters for the stability of MTMs/KBMs, and it is reduced by approximately a factor of $1/\kappa^2$ compared to a β_e when defined in terms of $\bar{B}$. This should be taken into account when the experimental β_e is compared to gyro-kinetic simulations.

In the linear simulations, the normalized wave numbers $k_\theta \rho_s$, are fixed to the given values in the tables III and IV. These wave numbers correspond to the most linearly unstable modes with the highest growth rates. These are the baseline cases in our study, and these param eters will be used unless otherwise stated. The so called generalized magnetohydrodynamic MHD parameter is defined as (see Ref. [25])

$$\alpha_{MHD} = -q^2 R_0 \frac{8\pi}{B_{unit}^2}\frac{dp}{dr} c_p, \tag{3}$$

where R_0 is the major radius of the centroid of the flux surface, and $p = \Sigma_a n_a T_a$ is the total plasma pressure. c_p is the geometric pressure gradient scaling parameter which allows an artificial adjustment of α_{MHD} without modifying the background gradients as presented in Ref. [26].

For a clearer comparison regarding the position of our selected discharges relative to the rest of the database presented in Ref. [11] (see Figs. 5(b) and 14), the confinement enhancement factor

$H_{98}(y, 2)$, density and temperature scale lengths as functions of normalized collision frequency, ν_{ei} (a/c_s), are shown in Fig.3. As seen in this figure for both radii, the two hybrid plasmas are located at low collisionality together with the low-δ baseline due to their lower density and higher temperature, while the high-δ baseline is located at high collisionality for both radii due to its high density and low temperature.

We note, that since the densities, the applied heating powers and total plasma currents are rather different in the cases considered the values of the normalized confinement factor $H_{98}(y, 2)$ may not be indicative of the plasma confinement in absolute units; in fact the baseline plasmas have higher confinement times than that of the hybrids for in the selected discharges. Nevertheless, to identify the reason for the good normalized confinement in hybrids is of great practical importance for development of high-gain scenarios in tokamak reactors.

Figures 3(b) and (c) show that the gradients of the electron density and ion temperature are highest in hybrids at the inner radius ($r/a = 0.3$). At the outer radius however, the high- baseline plasma shows the highest values. The low-δ baseline in comparison to both hybrid plasmas, also shows lower values for electron density and ion temperature gradients at the inner core radius, but at the outer radius these values are comparable to those of the hybrids. In the following sections we will investigate the stability of the selected plasmas to electrostatic and electromagnetic micro-instabilities and discuss the results and implications for the developments of the future operational scenarios.

3. LINEAR INSTABILITY ANALYSIS

In this section we present the results of our linear stability analysis with the GYRO code, including both shear- and compressional magnetic perturbations ($\delta B_\perp (= \nabla \times \delta A_\parallel)$ and $\delta B_\parallel$, respectively). Drift-kinetic electrons are assumed, and the collisions are modeled using an energy dependent Lorentz operator. Both electron-ion and electron-electron collisions are included in the electron collision frequency $\nu_e(v)$, and collisions between all ion species are accounted for. To take the plasma shape into account we have used a Miller-type local equilibrium model available in GYRO, see Refs. [23, 24].

Typical resolution parameters used in our linear analysis are as follows: 40 radial grid points, 12 parallel orbit mesh points (×2 signs of parallel velocity), 16 pitch angles, and 8 energies.

Figure 4 shows the growth rates γ and real frequencies ω of the most unstable linear modes as functions of $k_\gamma \rho_s$ for the selected discharges at both radii (the values are given in c_s/a units, with $c_s = (T_e/m_i)^{1/2}$ the ion sound speed). As shown in Fig.4(a) and (b), for the inner core region at r/a = 0.3, there is a difference in the nature of the underlying unstable modes between the hybrid and baseline plasmas. The most unstable modes in both hybrid plasmas are kinetic ballooning modes (KBMs), propagating in the ion diamagnetic direction (negative ω), while in the baseline plasmas we find unstable trapped electron mode (TEM) and micro-tearing mode (MTM) in the high-δ and the low-δ cases, respectively; these modes propagate in the electron diamagnetic direction (positive ω). However, in the outer core, at $r/a = 0.6$, ion temperature gradient (ITG) modes are the most unstable instabilities in all selected discharges, see Fig.4(c) and (d). The $\delta\phi$, $\delta A_\parallel$ and $\delta B_\parallel$ components

of the parallel eigenmode structure are shown in Figs. 5 and 6. The eigenfunctions are normalized so that $\delta A_{||}(\xi = 0)$ is unity. The MTM signature is distinguished by the odd (even) parity of the eigenfunction in ($A_{||}$), and correspondingly for KBMs the even (odd) parity of the eigenfunction in $\delta\phi$ ($\delta A_{||}$) eigenmodes [27]. Due to very low magnetic shear, the eigenmodes are very elongated along the field line in the inner core radius ($r/a = 0.3$) and therefore a very high radial resolution was needed (we used 40 radial grid pints) to resolve the modes. The above mentioned identification of the modes, is not purely based on the parities of their eigenmodes, but also on their dependencies on the various plasma gradient scaling lengths which will be discussed in the following sections.

Figure 7 illustrates the normalized linear heat and particle fluxes as functions of $k_\theta \rho_s$ for all the selected discharges. For the inner core radius, as seen in Fig. 7(a), KBMs in hybrid plasmas generate positive (outward) particle flux with the maximum located at the $k_\theta \rho_s$ corresponding to the maximum of their growth rates (see Fig. 4(a)). In the high-δ baseline TEMs generate negative (inward) particle flux at low $k_\theta \rho_s$ but the maximum particle flux is positive and located at $k_\theta \rho_s$ corresponding to the maximum growth rate (see Fig. 4(a)). In the low- baseline however, the MTM driven particle flux varies from negative to positive as $k_\theta \rho_s$ increases, and at the position of the $k_\theta \rho_s$ corresponding to the maximum growth rate the flux is close to zero. This is in agreement with the previous linear [12] and non-linear [17, 28] works where it was also shown that negligible levels of MTMs driven particle flux are expected.

The main channel of transport for KBMs in hybrid plasmas is the heat flux with slightly higher levels obtained for the ion heat flux, as shown in Figs. 7(b) and (c). As seen in these figures, the electron heat flux generated by TEM modes in low-δ baseline plasma is significantly higher than those generated by KBMs in the hybrids whereas the ion heat flux due to TEMs is negligibly small and close to zero. Note that for more clear view the values of the electron heat fluxes for the baseline plasmas in Fig.7(b) have been rescaled where the scaling parameters are 0.1 and 0.01 for the high and low-δ baseline plasmas, respectively. In the low-δ baseline plasma, the MTMs generate the highest level of the electron heat flux compared to the other three plasmas, as seen in Fig.7(b), while the ion heat flux as shown in Fig.7(c), is negligibly small. However, note that such high values of the MTM-driven electron heat flux is partly an artefact of the normalization of the linear fluxes, since the ratio of the perturbed electrostatic potential and the parallel vector potential $A_{||}$ is smaller for MTMs than for the other modes, while the electron heat flux is mostly $A_{||}$-driven "flutter" transport in that case.

For the outer core radius, as seen in Figs. 7(d-f), however, the particle and heat fluxes are driven by ITG modes in all the selected plasmas and show similar trends as $k_\theta \rho_s$ varies, with similar values obtained for all four studied discharges. In all the cases the particle fluxes generated by ITGs are positive and outward directed, with higher levels compare to those for the inner core radius, see Fig.7(d). Similarly the electron and ion heat fluxes generated by ITGs are higher than those obtained at $r/a = 0.3$ with the exception of the electron heat flux driven by MTMs in the low- baseline plasma, which is an order of magnitude higher.

A. SENSITIVITY SCANS FOR β_e AND α_{MHD}

In order to analyze the importance of the plasma pressure on the instability of electromagnetic modes, we performed β_e scans for the selected discharges at the two core radii, see Fig.8, where the experimental values of β_e are shown by vertical lines with similar colour coding to their corresponding curves. As seen in Figs.8(a) and (b) for the inner core radius in the hybrid plasmas (high-δ: red solid line, and low-δ: blue dashed line), in the absence of the electromagnetic effects ($\beta_e = 0$), we find that the most unstable modes are ITGs, and by including the electromagnetic effects the ITGs are stabilized, while the KBMs are destabilized and become the dominant instability with a very low β_e threshold: $\beta_e < 0.1\%$. In both hybrid plasmas, the KBM growth rate shows a non-monotonic change as the β_e is increased. After an initial phase of destabilization by β_e, the KBMs become stabilized by further increase in β_e. The stabilization is due to the increase in the α_{MHD} with β_e (see Eq. (3)), and is demonstrated in Fig.9, where the impact of α_{MHD} on the stabilization of the modes is examined. In this figure red (solid) lines represent the scans with self-consistent variation of the MHD with β_e and the blue (dashed) lines represent the scans in which by varying the c_p parameter as β_e varies (see Eq. (3)) we ensure that α_{MHD} is kept constant and equal to the corresponding experimental value given in tables I and II. As seen in Figs. 9(a,b) (high- hybrid) and (e,f) (low- hybrid) at $r/a = 0.3$ and bellow the experimental β_e values marked by the straight lines, the onset of the mode is moved to higher β_e, since the α_{MHD} is high and therefore the modes are stabilized. As β_e increases beyond the experimental values and because α_{MHD} is kept constant the growth rates increase strongly without any further stabilization.

As shown in Figs.8(a) and (b), in the high-δ baseline plasma (green dashed dotted lines) the growth rate of the TEM mode decreases with increasing β_e, but the TEM remains the dominant instability throughout the β_e scan. The stabilization due to α_{MHD} for the TEM mode is strong as seen in Figs.9(i) and (j). The MTMs in the low- baseline plasma (mauve dotted lines) shown in Figs.8(a) and (b), are destabilized for $\beta_e > 0.5\%$ and their growth rate increases with β_e, however above the experimental level of e the mode growth rate does not increase significantly. There is very little stabilization due to α_{MHD} on the MTM modes, as seen in Figs.9(m) and (n).

At the outer core radius ($r/a = 0.6$) ITG is the most unstable mode in all the selected plasmas, which is slightly stabilized with increasing β_e. The ITG growth rates are comparable to the values obtained in the absence of the electromagnetic effects ($\beta_e = 0$), see Figs.8(c) and (d). Also, as seen in Figs. 9(c,d) (high-δ hybrid), g,h (low-δ hybrid), k,l (high-δ baseline) and (o,p) (low-δ baseline), there is very little stabilization from α_{MHD} on the ITG modes and in the presence of constant α_{MHD}, while the KBMs are destabilized as e is increased above the experimental values.

B. SENSITIVITY TO PROFILE GRADIENTS AND COLLISIONALITY

In this section the results of our investigation on the impact of temperature and density gradients, and collisionality on the stability of the modes in the selected discharges are presented. Figures 10(a-h) show the $a/LT_{i,e}$ sensitivity studies at two radii. In all these scans α_{MHD} is kept constant and equal to the corresponding experimental values given in tables I and II. As seen in these figures,

by increasing a/LT_i the KBM (at $r/a = 0.3$) and ITG (at $r/a = 0.6$) are further destabilized, because a/LT_i is a drive for these modes. However, within 20 to 30% variation of a/LT_i the most unstable modes remain unchanged. On the other hand, for the TEM mode in high- baseline plasma (green dashed-dotted line), shown in Figs. 10(a) and (b), for a/LT_i similar to the experimental values in hybrid plasmas (shown with red and blue straight lines) the most unstable mode switches from a TEM to a KBM mode when the ion temperature gradient is increased sufficiently. This change is more visible in Fig. 10(b) were the real frequency of the mode changes from positive (electron direction) to negative (ion direction) with comparable values as in the hybrid KBMs (red solid and blue dashed lines). For the MTMs in low- baseline plasma (mauve dotted line), shown in Figs. 10(e) and (f), increasing a/LT_e results in destabilization of MTMs. However going to a/LT_e highly above the experimental level (represented by the mauve straight line) switches the most unstable mode from a MTM to a TEM, more clearly seen in Fig.10(f) were the real frequency shows a discontinuity with a significant reduction.

The sensitivity scans for density gradient scaling lengths, a/Ln_e, are shown in Figs. 11(ad). Here, quasi-neutrality is enforced by varying a/LN_i as a/Ln_evaries, while keeping the impurity density gradients fixed. In all these scans MHD is kept constant and equal to the corresponding experimental values given in tables I and II. For the high- hybrid plasma studied here (red solid lines in Figs. 11(a) and (b), and at $r/a = 0.3$, a mode change from TEM to KBM is observed when varying the a/Ln_e from negative to positive values (corresponding to a change in density profile from hallow to peaked, respectively). The mode change is observed around $a/Ln_e = 0$ (corresponding to a flat density profile), and the KBM growth rate is increased as a/Ln_e is increased i.e. the density profile becomes more peaked. Thus, in the inner core region of the hybrid plasma studied here, KBMs are expected to remain the dominant instability for a flat to peaked density profile. However, if the profile becomes hallow, the most unstable mode changes significantly and therefore, the expected transport characteristics are very different as well. No mode change is observed for the outer core radius, shown in Figs.11(c) and (d), and the main unstable mode remains an ITG mode for the whole a/Ln_e range considered with increasing growth rate as a/Ln_e is increased. Therefore, in this region further peaking of the density profile can result in an increase of the ITG driven transport.

In the high- baseline plasma (green dashed lines in Figs.11(a) and (b) the characteristics of the most unstable mode depends strongly on the density gradient scaling length. For the a/Ln_e bellow the experimental values (shown by the straight green dashed lines) TEMs remain the dominant instability however, as the a/Ln_e is increased i.e. more peaked density profile, the mode changes from a TEM to ITG and then to KBM. For the outer core region, similarly to the hybrid plasma case, the most dominant mode remains an ITG mode for the whole range of the scan with the growth rate slightly increasing as a/Ln_e is increased.

In the low-δ baseline plasma (mauve dashed-dotted lines in Figs.11(a) and (b) the MTMs remains the dominant instability for a range of $-0.2 < a/Ln_e < 0.2$, which correspond to a change from a slightly hallow to flat to slightly peaked density profile. Clearly a/Ln_e is not a strong and necessary drive for the MTMs, as there is a finite MTM growth rate at $a/Ln_e = 0$. However, as a/Ln_e is further

increased the mode changes from an MTM to a KBM. A transition from MTM to KBM with increasing a/Ln_e has also been reported previously in Refs. [12, 29, 30]. At the outer core radius, for both baseline plasmas, a mode change from TEM to ITG is observed as the a/Ln_e varies from negative to positive with a stronger variation seen in the case of the low- baseline plasma, see Figs. 11(c) and (d).

As was discussed in the previous section, collisionality between the hybrid and baseline plasmas are usually very different since baseline plasmas usually have higher electron density. Therefore, we have examined the role of collisionality in the stability properties of the these plasmas with respect to micro-instabilities. Figures 12(a-d) show the results of the collisionality scans for the two considered radii. Note that the plots are log-linear. At the inner core radius $r/a = 0.3$, the KBMs in hybrid plasmas show very little dependence to ν_{ei}, and are stabilized only at the very high ν_{ei}, however they remain KBM. The TEM mode in high- baseline plasma (green dashed-dotted line) also varies little with increase of collisionality, but MTM in low- baseline plasma (mauve dotted line) is unstable for very low ν_{ei} below its experimental value (represented by the mauve straight line) and shows a non-monotonic trend as ν_{ei} is increased, with the maximum around the experimental level. As was reported previously in the works [13, 31] the non-monotonic dependence of the MTM growth rate on collisionality is due to the fact that, on the one hand magnetic reconnection favours finite collisionality (although unstable MTMs have been found even in essentially collisionless cases [31, 32]), on the other hand, in a strong rate of scattering of electrons prevents the formation of a current layer, hence MTMs are stabilized at sufficiently high collisionality.

At the outer core radius $r/a = 0.6$, the ITGs in all the selected discharges are stabilized strongly as the collisionality is increased, as seen in Figs. 12(c) and (d). The reason for this strong stabilization is a collisional reduction of the non-adiabatic trapped electron response, as the destabilizing effect of the trapped electrons on ITG is well known, see Ref. [33]. The trapped electron response is mostly eliminated at $\nu_{ei} / |\omega| >> 1$, accordingly we observe that the growth rates level off around $\nu_{ei} \sim c_s/a$. The real part of the ITG mode frequency is only weakly affected by the collisions.

In summary, the results show that, in the hybrid plasmas, the most unstable modes regardless of their type, have higher growth rates than in the baseline plasmas. This is not surprising since gradients and therefore the drives of the KBM/ITG modes are higher, and collisionality which has stabilizing impact is lower in the hybrid plasmas, see tables I-IV. However, experimentally, the hybrids show better core confinement than baseline plasmas, which would suggest presence of a lower level of turbulent transport. Thus, we expect that the experimental cases correspond to stable or only marginally unstable situations. Therefore the resolution of this apparent contradiction requires additional physics to be considered as will be shown below, and there is a reason to believe that the set of geometry and profile parameters used here may be somewhat different from the actual experimental ones, and a strong sensitivity for some of these parameters may account for the stability of the experimental cases. In the following section we will examine the role of possible stabilizing mechanisms in the selected plasmas.

C. ROLE OF FAST IONS, SAFETY FACTOR AND MAGNETIC SHEAR ON THE STABILITY OF THE MODES

Figures 13(a-h) show the results of magnetic shear s and safety factor q scans for the selected discharges at both radii. As seen in Figs. 13(a,b) and (e,f) for the inner core region (r/a = 0.3), variation in s and q have significant impact on the stability of the KBMs in the hybrids while they have only minimal effect on stability of TEM and MTM in the baseline plasmas. A non-monotonic variation with q is observed for KBM growth rates as shown in Figs.13(e,f), with the peak being around the experimental values (shown with vertical bars). However within the range of q variation considered here, KBM remains the dominant instability with decreased growth rate as q is increased. As illustrated in Figs.13(a,b), the low magnetic shear in hybrids ($s \sim 0.01$) is a reason for the destabilization of the KBMs since by increasing the shear towards the baseline values ($s \sim$ 0.1) the KBMs are completely stabilized and the most unstable mode would switch to ITG type in both hybrid plasmas. The importance of low magnetic shear in destabilization of the KBMs is further investigated by a series of β_e scans at various s, for the two hybrid plasmas, presented in Figs.14(a-d). As shown here, the very low magnetic shear in hybrids results in the observed low β_e threshold of KBMs in these plasmas, and as s is increased the threshold is pushed towards higher β_e. Hence, it is not surprising that although baselines plasmas have similar experimental β_e (see tables I) to those of hybrids, because of their higher magnetic shear, they are KBM stable. This suggests that from inner core instability point of view an important parameter in hybrid plasmas is the low magnetic shear.

As seen in Figs.13(c,d) and (g,h), for the outer core radii (r/a = 0.6), an increase in either magnetic shear or safety factor will result in stabilization of the ITG modes in all selected plasmas. However, with variations in a realistic uncertainty range, the ITG mode remains the dominant instability and is not completely stabilized.

An important stabilizing parameter for the core micro-instabilities, is the pressure gradient, $\beta' \sim dp/dr$, or α_{MHD} parameter. It has been shown previously that in the so-called $s - \alpha$ equilibrium which is valid at high β and very large aspect ratio for circular concentric magnetic surfaces; the high pressure gradient reduces the magnetic drift drive responsible for the interchange instability, see Ref. [34]. However, in the case of the Miller equilibrium considered here, the effect of the pressure gradient on the drift velocity is complicated, see Ref. [25]. The increase in pressure gradient can be the result of the presence of a minority of energetic ions, and previous works have shown their importance on the suppression of ITG modes driven by gradients of the thermal population (deuterium) [35]. Also, the impact of fast ion dilution of the main ion species have been reported in Refs. [36, 37], and recent nonlinear electromagnetic simulations of JET experimental discharges have shown strong stabilization by supra-thermal pressure gradients to be a key factor in reducing tokamak ITG instabilities [38].

Therefore, we have examined the impact of the fast ion population on micro-instabilities in the core of the hybrid high-δ discharge (Pulse No: 77922), by considering the fast ions as a new ion species and using their density and temperature profiles calculated by TRANSP. The increase in

α_{MHD} parameter, due to fast ion population, is calculated to be around 20%, see Figs.15(a-d). In this figure, the red solid lines represent the results without the contribution from the fast ions, and square (mauve) symbols represent the results where the contribution from fast ions have been included. As seen here at $r/a = 0.3$, a 20% increase in α_{MHD} significantly suppresses the KBM however, this increase is not enough to completely stabilize the mode. At $r/a = 0.6$, however, this increase has no significant impact on the stability of the ITG mode.

In order to examine the sensitivity of these results to the fast ion population and therefore, on the α_{MHD}, we have artificially increased α_{MHD} using the multiplier parameter c_p as defined in Eq.3. The results are shown in Figs. 15(a-d) with black circle (MHD + 30%) and blue triangular (MHD + 50%) symbols. Again, these increases seem to significantly stabilize the KBM, but their impacts on ITG mode are minimal. These results indicate that the impact of the fast ions on the stabilization of the micro-instabilities is more relevant at the inner core radii, and is not expected to impact the modes further out. This is more clearly shown in Figs.16(a-f), where the results of β_e scans at various c_p values for three of the selected plasmas at the $r/a = 0.3$ are illustrated. For both hybrid plasmas, an increase in c_p results in a very strong suppression of the KBMs, and even a change to ITG mode seen in case of low-δ hybrid. However, the lower e threshold of the KBMs do not vary much as $c_p$is increased. In the case of low-δ baseline plasma, the increase in c_p does not result in significant suppression of the MTM, see Figs.16(e) and (f).

In summary, our findings show the importance of the fast ion contribution to the MHD and of the magnetic shear s on the onset and the stability of electromagnetic modes at the inner core radius in the selected hybrid discharges. We find that flat q-profiles in hybrid plasmas and therefore, the low magnetic shear can result in a shift of the β_e threshold of the electromagnetic modes like KBMs towards very low β_e in these plasmas. However, a strong suppression of KBMs due to the presence of fast ions can be expected for the inner core region. In the baseline plasmas however, neither the magnetic shear or fast ion contributions to the α_{MHD}, seem to result in a significant suppression of MTM/TEM modes. Thus, the good core confinement observed at $r/a = 0.3$ in the selected hybrid plasmas, can perhaps be explained as a result of a combination of these two effects: low magnetic shear and fast ions. Ref. [38] also reports that the nonlinear electromagnetic stabilization due to fast ions is seen to be more effective at low magnetic shear.

At the outer core radius ($r/a = 0.6$), the picture is different since the ITG modes here, are not strongly stabilized by fast ion contributions or variations of the magnetic shear and q. An important stabilizing factor in this region however, is the $\boldsymbol{E}\times\boldsymbol{B}$ flow shear, and hence, we have investigated the impact of the flow shear in a series of local non-linear simulations at various radii for three of the selected discharges. The results are presented in the following section.

4. NON-LINEAR ANALYSIS AND THE IMPACT OF E×B

In this section the effects of $\boldsymbol{E}\times\boldsymbol{B}$ flow shear have been investigated in non-linear electromagnetic gyro-kinetic turbulence simulations with GYRO code. These runs including both shear- and compressional magnetic perturbations: $\delta \mathrm{B}_{\perp}$ and $\delta \mathrm{B}_{\parallel}$, respectively. We use a 128-point velocity

space discretizations (8 pitch angles, 8 energies, and 2 signs of velocity). 16 toroidal mode numbers were used. The maximum $k_\theta \rho_s = 0.8$ used in all simulations , except for the baseline high-δ case where the maximum $k_\theta \rho_s = 2.5$ was used. The simulation time was sufficiently long to achieve statistically steady-state levels with adequate time stepping and box sizes. We have also performed convergence tests which establish the adequacy of the time step and box size.

The non-linear heat and particle fluxes calculated by local non-linear GYRO simulations for three of the selected plasmas are shown in Figs.17(a-i). The results are shown for cases with and without taking into account the effect of flow shear.

As can be seen in Figs.17(a-f), for $r/a < 0.5$ core region, the non-linear fluxes are significantly higher in hybrid plasmas when flow shear effects are taken into account (redsolid lines), in comparison to the case where these effects are excluded (dashed blue lines). The higher fluxes in these plasmas are due to destabilization by Parallel Velocity Gradients (PVG) on the KBM/ITG modes in this region. Using that in GYRO the effects of parallel and the perpendicular flow shear can be changed independently we could investigated this effect further for the $r/a = 0.3$ in hybrid high-δ plasma by artificially taking out the contribution from PVG. Indeed, we find that when these effects are not included, the fluxes are similar to those obtained without considering the full **E×B** effects. The destabilization impact of PVG on ITG modes have been reported previously, where it has been shown that in the presence of a large p the transport may not be quenched by **E×B** shear, see Refs. [39, 40]. Recent studies presented in Ref. [38] also, show destabilization of the ITG modes due to PVG in the core of JET plasmas.

However, PVG destabilizing impact decreases with decreasing geometrical factor Rq/r [41], and therefore, the **E×B** shear can be expected to strongly stabilizes the turbulence in the outer core region and indeed as can be seen in Figs.17(a-c), in hybrid high-δ at $r/a = 0.6$ the turbulence fluxes are significantly reduced. The **E×B** shear in the baseline high- plasma also has stabilizing impact on the turbulence for all considered radii ($r/a = 0.3$ and 0.6), see Figs. 17(g-i).

CONCLUSIONS

The experimental observations show that Hybrid plasmas can have significantly improved normalized confinement above the standard $H_{98}(y; 2)$ H-mode scaling. However, the underlying physics basis for the observed increased normalized confinement remained somewhat unclear. Confinement properties of a database of 112 plasmas in JET with CFC wall were analyzed in Ref. [11], and it was shown that the improved confinement in the hybrid discharges were partly due to better core confinement in these plasmas. Therefore here, the confinement improvement due to stabilization of the micro-turbulence driven transport has been tested in a selected subset of two hybrid and two baseline experimental discharges from the database, using local linear and non-linear gyro-kinetic simulations with the gyro code [19, 20]. The characteristics and the onset of electromagnetic micro-instabilities at two core radii ($r/a = 0.3$ and 0.6) are analyzed through a series of sensitivity scans for various plasma parameters.

The results show that in the inner core ($r/a = 0.3$) the characteristics of the dominant unstable

modes in the selected hybrid and baseline plasmas are very different, with KBMs unstable in hybrids and MTM/TEM modes unstable in baselines. For the outer core ($r/a = 0.6$), however, ITGs are found to be the dominant instability in all the selected discharges. The linear growth rates of the dominant instabilities are found to be higher in the hybrid plasmas than in baselines due to lower collisionality, higher temperature and density gradients in these plasmas. Variation of these parameters within a wide range does not result in complete stabilization of the unstable core KBMs in hybrids. However, in the inner core of the selected hybrid discharges our findings show the importance of α_{MHD}-stabilization of electromagnetic instabilities in the presence of low magnetic shear. We find that the flat q-profiles in hybrid plasmas and the corresponding very low magnetic shear can result in a shift of the β_e threshold of the electromagnetic modes like KBMs towards very low es in these plasmas. However, a strong suppression of KBMs due to the presence of fast ions can be expected for the inner core region. In the baseline plasmas however, neither the magnetic shear or fast ion contributions to the α_{MHD}, result in a significant suppression of MTM/TEM modes. Thus, the good core confinement observed at $r/a = 0.3$ in the selected hybrid plasmas, can perhaps be explained as a result of a combination of these two effects: low magnetic shear and the fast ion stabilization of KBMs. Comparing the non-linear heat fluxes computed by GYRO and obtained by power balance analysis with TRANSP for the inner core region show larger disagreement with higher values computed by GYRO, than for the outer region. As it was shown in Ref. [38] stabilisation of the ITG modes due to fast ions can be even more efficient non-linearly, therefore, we suspect that also for the KBMs found in this region, the inclusion of the fast ions will result in a more significant stabilisation of the modes non-linearly and better agreement with fluxes obtained by TRANSP.

In the outer core ($r/a = 0.6$), the picture is different, since the ITG modes there are not strongly stabilized by fast ion contributions, and variation in the magnetic shear and q have non-monotonic effect on the stability of the modes, with the peak being around the experimental values. An important stabilizing mechanism in this region however, is found to be the **E×B** shear. This effect was investigated in a series of local non-linear simulations, where we find a significant stabilization of the ITG modes due to **E×B** shear, and therefore, a strong quench of the turbulence transport can be expected in this region. For the inner core radius, however, non-linear simulations show destabilization of KBMs with **E×B** shear due to the presence of a large PVG effect. The impact of PVG on the destabilization of ITG modes has been reported previously in Refs. [38–40], however, their impact on the destabilization of KBMs is reported here for the first time, and further studies of this effect is ongoing.

In summary, a good inner core confinement due to strong stabilization of the microturbulence driven transport can be expected in the hybrid plasmas as a result of stabilization by the fast ion pressure which is more effective at low magnetic shear due to q-profile optimization achieved in the hybrid plasmas. For the outer core radii the hybrid plasmas may benefit from a strong reduction of turbulent transport by **E×B** rotational shear, as was reported in Ref. [42, 43].

ACKNOWLEDGMENTS

The authors would like to thank J Candy for providing the gyro code. This work was funded by the European Communities under Association Contract between EURATOM and CEA. The views and opinions expressed herein do not necessarily reflect those of the European Commission. Computational resources of the High Performance Computing for Fusion (HP-FF) facility were used for nonlinear gyrokinetic simulations. IPA is grateful for the financial support of Vetenskapsrådet.

REFERENCE

[1]. F. Romanelli et al. Proc. 24th Int. Conf. on Fusion Energy (2012) (San Diego, USA, 2012) paper OV/1-3. www-naweb.iaea.org/napc/physics/FEC/FEC2012/index.htm.

[2]. M. Shimada, D.J. Campbell, V. Mukhovatov, M. Fujiwara, N. Kirneva, K. Lackner, M. Nagami, V.D. Pustovitov, N. Uckan and J. Wesley International Tokamak Physics Activity Topical Group Chairs, Cochairs and Chapter Coordinators: N. Asakura, A.E. Costley, A.J.H. Donné, E.J. Doyle, A. Fasoli, C. Gormezano, Y. Gribov, O. Gruber, T. C. Hender, W. Houlberg, S. Ide, Y. Kamada, A. Leonard, B. Lipschultz, A. Loarte, K. Miyamoto, V. Mukhovatov, T.H. Osborne, A. Polevoi and A.C.C. Sips, Progress in the ITER Physics Basis Chapter 1: Overview and summary, Nuclear Fusion **47**, S1 (2007).

[3]. D.C. McDonald, L. Laborde, J.C. DeBoo, F. Ryter, M. Brix, C.D. Challis, P. de Vries, C. Giroud, J. Hobrik, D. Howell, E. Joffrin, T.C. Luce, J. Mailloux, V. Pericoli-Ridolfini, A.C. C. Sips, K. Thomsen and JET EFDA Contributors, Plasma Physics and Controlled Fusion **50**, 124013 (2008).

[4]. C. Gormezano, A. Becoulet, P. Buratti, L. Carraro, F. Crisanti, B. Esposito, G. Giruzzi, R. Guirlet, G. T. Hoang, E. Joffrin, X. Litaudon, T. Luce, V. Pericoli-Ridolfini, O. Sauter, A. C. C. Sips, A. Tuccillo and the JET EFDA Contributors, Plasma Physics and Controlled Fusion **46** B435 (2004).

[5]. C. Gormezano, A.C.C. Sips, T.C. Luce, S. Ide, A. Becoulet, X. Litaudon, A. Isayama, J. Hobirk, M.R. Wade, T. Oikawa, R. Prater, A. Zvonkov, B. Lloyd, T. Suzuki, E. Barbato, P. Bonoli, C.K. Phillips, V. Vdovin, E. Joffrin, T. Casper, J. Ferron, D. Mazon, D. Moreau, R. Bundy, C. Kessel, A. Fukuyama, N. Hayashi, F. Imbeaux, M. Murakami, A.R. Polevoi and H.E. St John, Progress in the ITER physics basis. Chapter 6: steady state operation Nuclear Fusion **47** S285 (2007).

[6]. R.J. Buttery, T.C. Hender, D.F. Howell, R.J. La Haye, O. Sauter, D. Testa and contributors to the EFDA-JET Work programme, Nuclear Fusion **43** 69 (2003).

[7]. E. Joffrin, A.C.C. Sips, J.F. Artaud, A. Becoulet, L. Bertalot, R. Budny, P. Buratti, P. Belo, C.D. Challis, F. Crisanti, M. de Baar, P. de Vries, C. Gormezano, C. Giroud, O. Gruber, G.T.A. Huysmans, F. Imbeaux, A. Isayama, X. Litaudon, P.J. Lomas, D.C. McDonald, Y.S. Na, S.D. Pinches, A. Staebler, T. Tala, A. Tuccillo, K.-D. Zastrow and JET-EFDA Contributors to the Work Programme, Nuclear Fusion **45** 626 (2005).

[8]. E. Joffrin, C. Challis, J. Critin, J. Garcia, J. Hobirk , I. Jenkins, J. Lonnroth, D.C. McDonald,

P. Maget , P. Mantica, M. Beurskens, M. Brix, P. Buratti, F. Crisanti, L. Frassinetti, C. Giroud, F. Imbeaux, M. Piovesan, F. Rimini, G. Sergienko, A.C.C. Sips, T.Tala, I. Voitsekovtich and JET-EFDA Contributors, Proc. 23rd Int. Conf. on Fusion Energy 2010 (Daejeon, South Korea, 2010) (Vienna IAEA) CD-ROM file EXC/1-1 and wwwnaweb. iaea.org/napc/physics/FEC/FEC2010/html/index.htm.

[9]. J. Hobirk, F. Imbeaux, F. Crisanti, P. Buratti, C.D. Challis, E. Joffrin, B. Alper, Y. Andrew, P. Beaumont, M. Beurskens, A. Boboc, A. Botrugno, M. Brix, G. Calabro, I. Coffey, S. Conroy, O. Ford, D. Frigione, J. Garcia, C. Giroud, N.C. Hawkes, D. Howell, I Jenkins, D. Keeling, M. Kempenaars, H. Leggate, P. Lotte, E. de la Luna, G.P. Maddison, P. Mantica, C. Mazzotta, D.C. McDonald, A. Meigs, I. Nunes, E. Rachlew, F. Rimini, MSchneider, A.C.C Sips, J. K. Stober, W. Studholme, T. Tala, M. Tsalas, I. Voitsekhovitch, P. C. de Vries and JET-EFDA contributors, Plasma Physics and Controlled Fusion **54** 095001 (2012).

[10]. ITER Physics Basis Expert Groups on Confinement and Transport and Confinement Modelling and Database, ITER Physics Basis Editors, Nuclear Fusion **39** 2175 (1999).

[11]. M. N. A Beurskens, L. Frassinetti, C. Challis, T. Osborne, P.B. Snyder, B. Alper, C. Angioni, C. Bourdelle, P. Buratti, F. Crisanti, E. Giovannozzi, C. Giroud, R. Groebner, J. Hobirk, I. Jenkins, E. Joffrin, M.J. Leyland, P. Lomas, P. Mantica, D. McDonald, I. Nunes, F. Rimini, S. Saarelma, I. Voitsekhovitch, P. de Vries, D. Zarzoso and JET-EFDA Contributors, Nuclear Fusion **53** 013001 (2013).

[12]. S. Moradi, I. Pusztai, W. Guttenfelder, T. Fülöp and A. Mollén, Nuclear Fusion **53** 063025 (2013).

[13]. S. Moradi, I. Pusztai, A. Mollén and T. Fülöp, Physics of Plasmas **19** 032301 (2012).

[14]. M. J. Pueschel, M. Kammerer, and F. Jenko, Physics of Plasmas 102310 (2008).

[15]. M. J. Pueschel and F. Jenko, em Physics of Plasmas **17** 062307 (2010).

[16]. A. Ishizawa, S. Maeyama, T.-H. Watanabe, H. Sugama and N. Nakajima, Nuclear Fusion **53** 053007 (2013).

[17]. W. Guttenfelder, J. Candy, S.M. Kaye, W.M. Nevins, E. Wang, R.E. Bell, G.W. Hammett, B.P. LeBlanc, D.R. Mikkelsen and H. Yuh, Physical Review Letters **106** 155004 (2011).

[18]. H. Doerk, F. Jenko, M.J. Pueschel and D.R. Hatch, Physical Review Letters **106** 155003 (2011).

[19] J. Candy and R.E. Waltz, Journal of Computational Physics, **186** 545 (2003).

[20]. J. Candy and E. Belli, General Atomics Report GA-A26818 (2011).

[21]. R.J. Goldston, D.C. McCune, H.H. Towner et al, Journal of Computational Physics **43** 61 (1981).

[22]. L.L. Lao et al, Nuclear Fusion **30** 1035 (1990).

[23]. R.E. Waltz and R.L. Miller, Physics of Plasmas **6**, 4265 (1999).

[24]. J. Candy, Physics of Plasmas **12** 072307 (2005).

[25]. J. Candy, Plasma Physics and Controlled Fusion, **51** 105009 (2009).

[26]. E.A. Belli and J. Candy, Physics of Plasmas, **17** 112314 (2010).

[27]. D.R. Hatch, M.J. Pueschel, F. Jenko, W.M. Nevins, P.W. Terry, and H. Doerk, Physics of Plasmas **20**, 012307 (2013).
[28]. W. Guttenfelder, J. Candy, S.M. Kaye, W.M. Nevins, E. Wang, J. Zhang, R.E. Bell, N.A. Crocker, G.W. Hammett, B.P. LeBlanc, D.R. Mikkelsen, Y. Ren and H. Yuh, Physics of Plasmas **19** 056119 (2012).
[29]. W. Guttenfelder, J. Candy, S.M. Nevins, R.E. Bell, G.W. Hammett, B.P. LeBlanc and H. Yuh, Physics of Plasmas **19**, 022506 (2012).
[30]. D. Dickinson, C.M. Roach, S. Saarelma, R. Scannell, A. Kirk, and H.R. Wilson, Physical Review Letters **108**, 135002 (2012).
[31]. H. Doerk, F. Jenko, T. Görler, D. Told, M.J. Pueschel and D.R. Hatch, Physics of Plasmas **19**, 055907 (2012).
[32]. D. Carmody, M.J. Pueschel and P.W. Terry, Physics of Plasmas **20** 052110 (2013).
[33]. M. Romanelli, G. Regnoli and C. Bourdelle, Physics of Plasmas **14**, 082305 (2007).
[34]. C. Bourdelle, W. Dorland, X. Garbet, G. W. Hammett, M. Kotschenreuther, G. Rewoldt and E. J. Synakowski, Physics of Plasmas **10** 2881 (2003).
[35]. M. Romanelli, A. Zocco, F. Crisanti and JET-EFDA Contributors, Plasma Physics and Controlled Fusion **52** 045007 (2010).
[36]. G. Tardini, J. Hobirk, V.G. Igochine, C.F. Maggi, P. Martin, D. McCune, A.G. Peeters, A.C.C. Sips, A. Stäbler, J. Stober and the ASDEX Upgrade Team, Nuclear Fusion **47** 280 (2007).
[37]. C. Holland, L. Schmitz, T.L. Rhodes, W.A. Peebles, J.C. Hillesheim, G. Wang, L. Zeng, E.J. Doyle, S.P. Smith, R. Prater, K.H. Burrell, J. Candy, R.E. Waltz, J.E. Kinsey, G.M. Staebler, J.C. DeBoo, C.C. Petty, G.R. McKee, Z. Yan and A.E. White, Phys. Plasmas 18 056113 (2011).
[38]. J. Citrin et al. Physical Review Letters **111** 155001 (2013).
[39]. J.E. Kinsey, R.E. Waltz, and J. Candy, Physics of Plasmas **12** 062302 (2005).
[40]. M. Barnes, F.I. Parra, E.G. Highcock, A.A. Schekochihin, S.C. Cowley, and C.M. Roach, Physical Review Letters **106** 175004 (2011).
[41]. E.G. Highcock, A.A. Schekochihin, S.C. Cowley, M. Barnes, F.I. Parra, C.M. Roach, and W. Dorland, Physical Review Letters **109** 265001 (2012).
[42]. X. Litaudon, I. Voitsekhovitch, J.F. Artaud, P. Belo, João, P.S. Bizarro, T. Casper, J. Citrin, E. Fable6, J. Ferreira, J. Garcia, L. Garzotti, G. Giruzzi, J. Hobirk, G.M.D. Hogeweij, F. Imbeaux, E. Joffrin, F. Koechl, F. Liu, J. Lönnroth, D. Moreau, V. Parail, M. Schneider, P.B. Snyder, the ASDEX-Upgrade Team, JET-EFDA Contributors and the EU-ITM ITER Scenario Modelling Group, Nuclear Fusion **53** 073024 (2013).
[43]. I. Voitsekhovitch et al, submitted to Nuclear Fusion (2013).

	B_{unit}	β_e	α_{MHD}	s	q	κ	δ	s_δ	s_κ
77922 (Hyb high-δ)	2.86	0.01	0.19	0.012	1.06	1.290	0.028	0.028	-0.0043
75225 (Hyb low-δ)	2.56	0.0097	0.26	0.062	1.09	1.357	0.03	0.027	-0.012
76679 (BL high-δ)	3.76	0.0085	0.11	0.14	1.17	1.39	0.041	0.045	0.014
78682 (BL low-δ)	2.90	0.012	0.07	0.12	1.05	1.4	0.033	0.036	0.008

Table I: Input parameters for plasma shape and magnetic geometry at r/a = 0.3.

	B_{unit}	β_e	α_{MHD}	s	q	κ	δ	s_δ	s_κ
77922 (Hyb high-δ)	3.05	0.0049	0.16	1.05	1.34	1.3	0.063	0.1	0.055
75225 (Hyb low-δ)	2.78	0.0044	0.21	1.08	1.46	1.35	0.065	0.1	0.045
76679 (BL high-δ)	4.06	0.0039	0.14	0.7	1.48	1.43	0.1	0.15	0.078
78682 (BL low-δ)	3.10	0.006	0.2	0.62	1.3	1.43	0.08	0.11	0.052

Table II: Input parameters for plasma shape and magnetic geometry at r/a = 0.6.

	Z_{eff}	$n_e[10^{19}/m^3]$	T_e[keV]	a/L_{ne}	a/L_{Ti}	a/L_{Te}	T_i/T_e	$\nu_{ei}(a/c_s)$	$k_\theta\rho_s$
77922 (Hyb high-δ)	1.53	5.4	3.9	0.66	1.34	1.38	1.48	0.028	0.3
75225 (Hyb low-δ)	1.37	3.96	4.1	0.8	1.86	1.3	1.77	0.02	0.15
76679 (BL high-δ)	1.83	11.0	2.9	0.22	0.84	1.43	1.14	0.11	1.5
78682 (BL low-δ)	1.9	6.25	4.1	-0.18	1.13	1.	1.05	0.03	0.45

Table III: Input parameters for densities, temperatures and their gradients at r/a = 0.3.

	Z_{eff}	$n_e[10^{19}/m^3]$	T_e[keV]	a/L_{ne}	a/L_{Ti}	a/L_{Te}	T_i/T_e	$\nu_{ei}(a/c_s)$	$k_\theta\rho_s$
77922 (Hyb high-δ)	1.53	4.35	2.6	0.94	2.1	1.16	1.22	0.051	0.3
75225 (Hyb low-δ)	1.37	3.96	4.1	1.25	2.1	1.2	1.4	0.033	0.3
76679 (BL high-δ)	1.83	9.5	1.7	0.4	2.5	1.7	1.1	0.25	0.3
78682 (BL low-δ)	1.9	5.7	2.5	1.15	2.1	2.26	1.	0.07	0.3

Table IV: Input parameters for densities, temperatures and their gradients at r/a = 0.6.

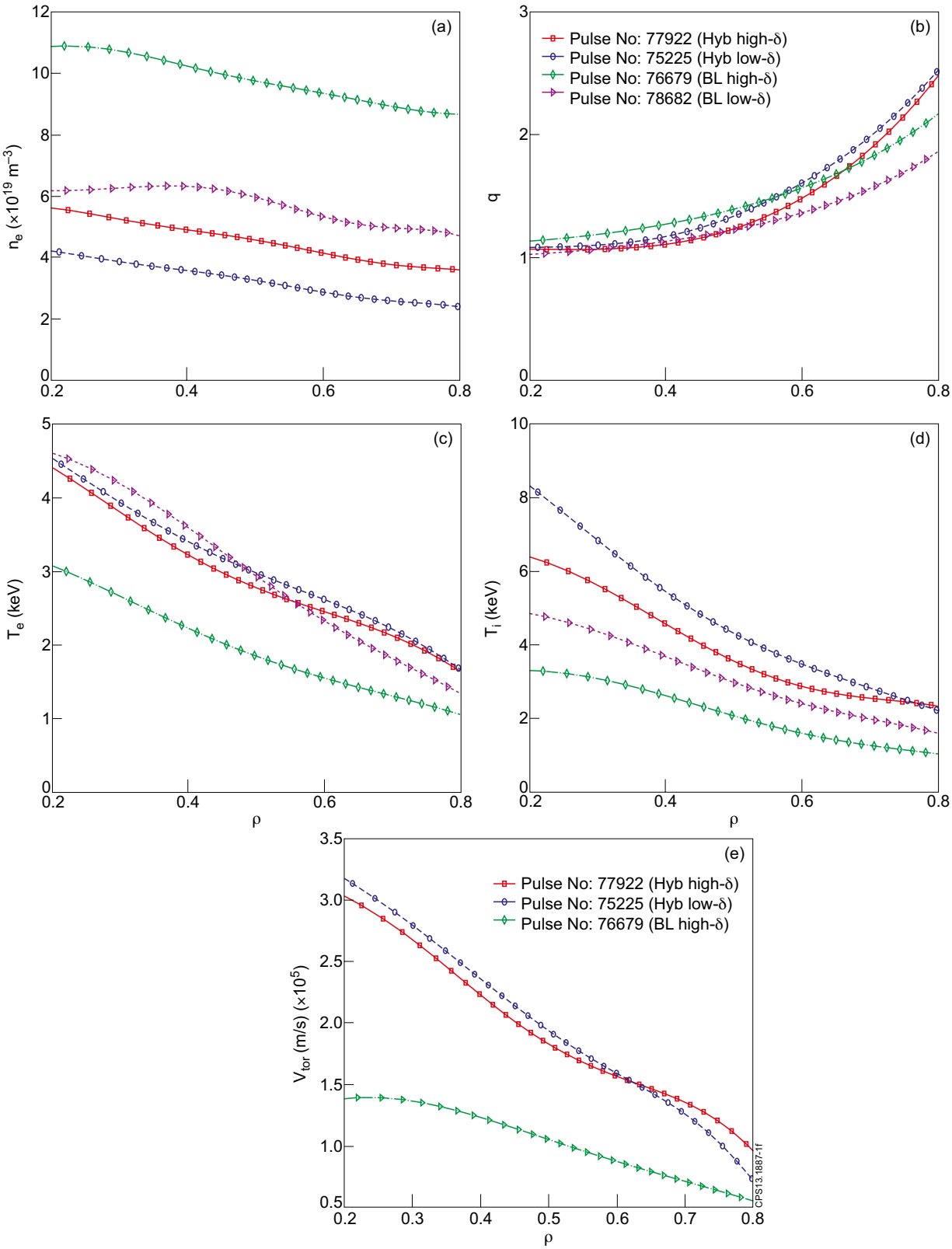

Figure 1: Input profiles: (a) electron density, (b) safety factor, (c) electron temperature, (d) ion temperature, and (e) toroidal rotation velocity calculated by TRANSP code. Solid (red) lines show the profiles for JET Pulse No: 77922, dashed (blue) lines for Pulse No: 75225, dashed-dotted (green) lines for Pulse No: 76679, and dotted (mauve) lines for Pulse No: 78682.

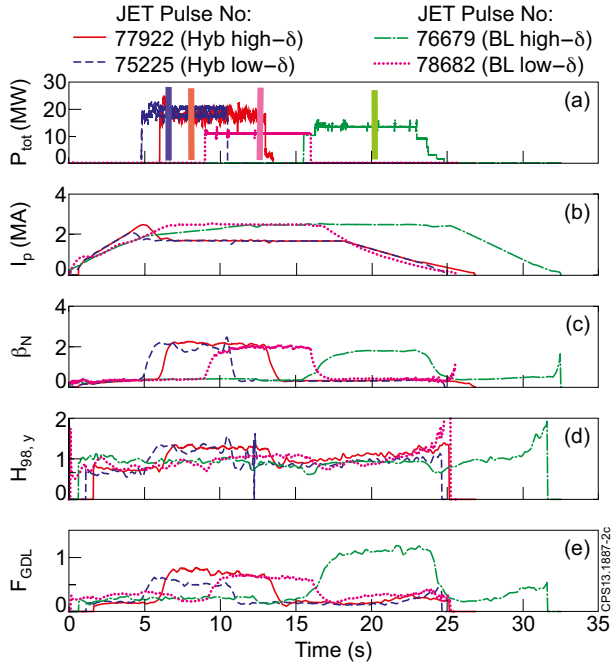

Figure 2: Time traces of main plasma parameters: (a) total input NBI power P_{tot}, (b) plasma current I_P, (c) normalized thermal pressure β_N, (d) the global confinement enhancement factor $H_{98}(y, 2)$ and (e) the Greenwald density fraction FGDL. Solid (red) lines show the values for JET Pulse No: 77922, dashed (blue) lines for Pulse No: 75225, dashed-dotted (green) lines for Pulse No: 76679, and dotted (mauve) lines for Pulse No: 78682. The highlighted bars in (a) denote the time periods for which the profiles were averaged over, and are color coded similarly to their corresponding curves.

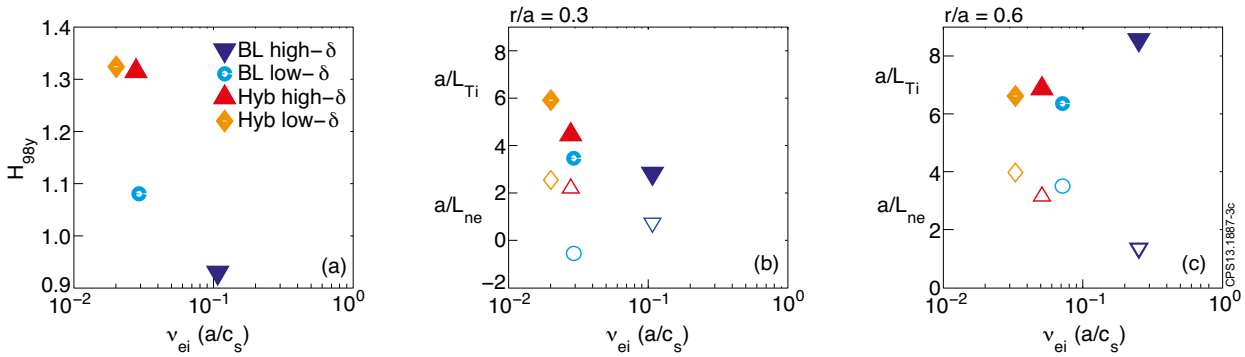

Figure 3: (a) Confinement factor $H_{98}(y, 2)$, and input density (open symbols) and temperature (full symbols) gradients versus collision frequency ei, (b) at inner core radius r/a = 0.3, and (c) at outer core radius r/a = 0.6. The down-triangles (dark blue) correspond to the values from the JET Pulse No: 76679, circles (light blue) for Pulse No: 78682, up-triangles (red) for Pulse No: 77922, and diamonds (brown) correspond to the values from Pulse No: 75225.

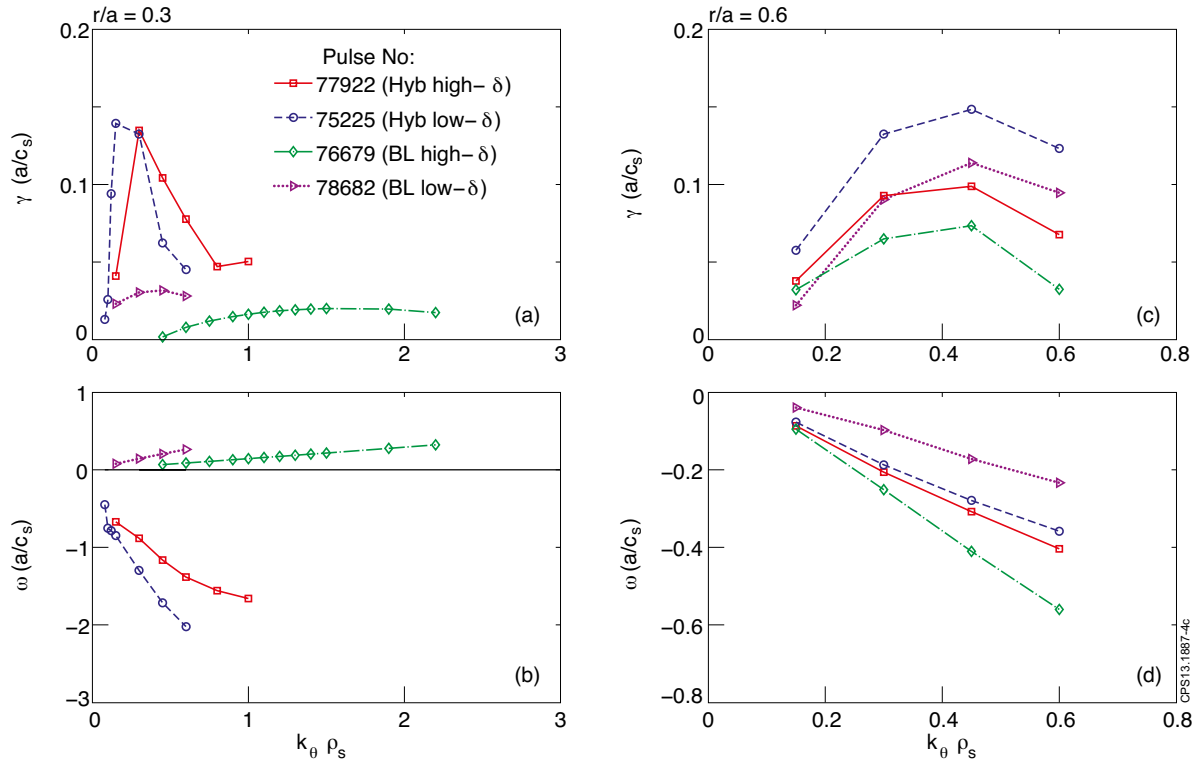

Figure 4: Imaginary and real frequency of the most linearly unstable modes as functions of $k_\theta \rho_s$ (a,b) at r/a = 0.3, and (c,d) at r/a = 0.6. Solid (red) lines correspond to the values for Pulse No: 77922, dashed (blue) lines for Pulse No: 75225, dashed-dotted (green) lines for Pulse No: 76679, and dotted (mauve) lines for Pulse No: 78682.

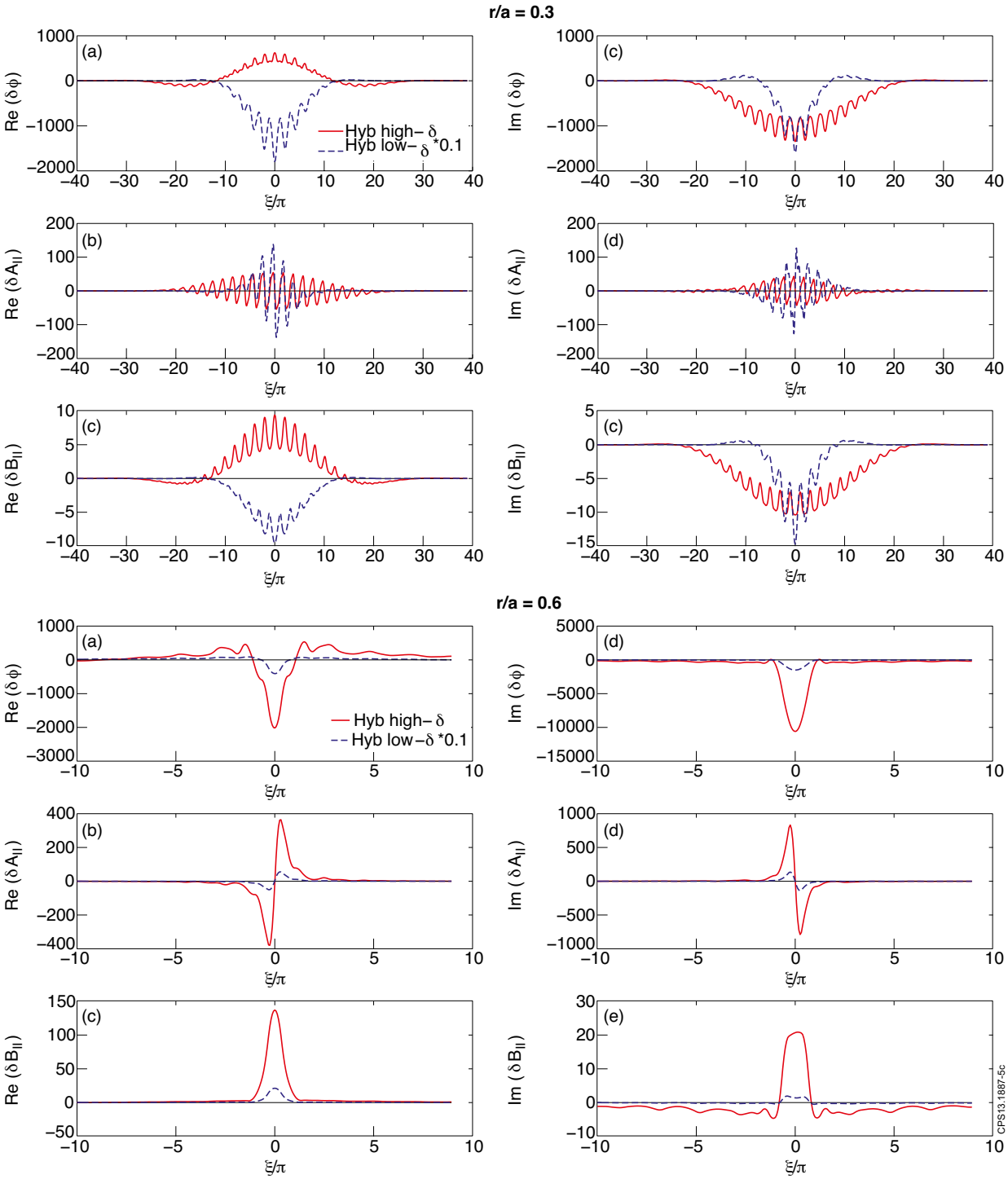

Figure 5: Linear parallel mode structures of $\delta\phi$, $\delta A_{||}$, and $\delta B_{||}$ as functions of the normalized extended poloidal angle ξ/π for hybrid plasmas. Top figures show the values for r/a = 0.3, and bottom figures show the values for r/a = 0.6. Solid (red) lines correspond to the values for Pulse No: 77922, dashed (blue) lines for Pulse No: 75225.

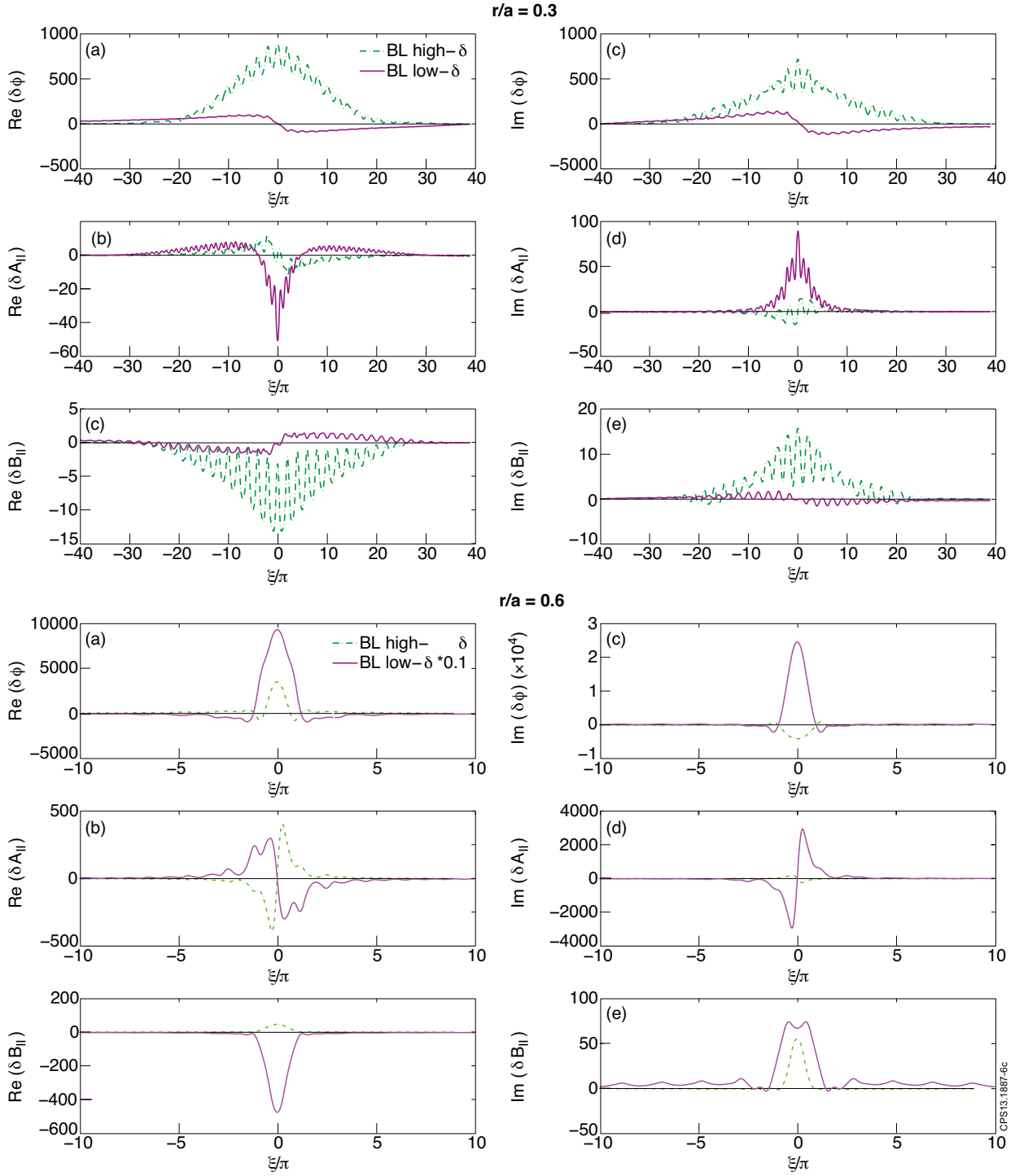

Figure 6: Linear parallel mode structures of $\delta\phi$, $\delta A_{||}$, and $\delta B_{||}$ as functions of the normalized extended poloidal angle ξ/π in baseline plasmas. Top figures show the values for r/a = 0.3, and bottom figures show the values for r/a = 0.6. Dashed-dotted (green) lines for Pulse No: 76679, and dotted (mauve) lines for Pulse No: 78682 discharges.

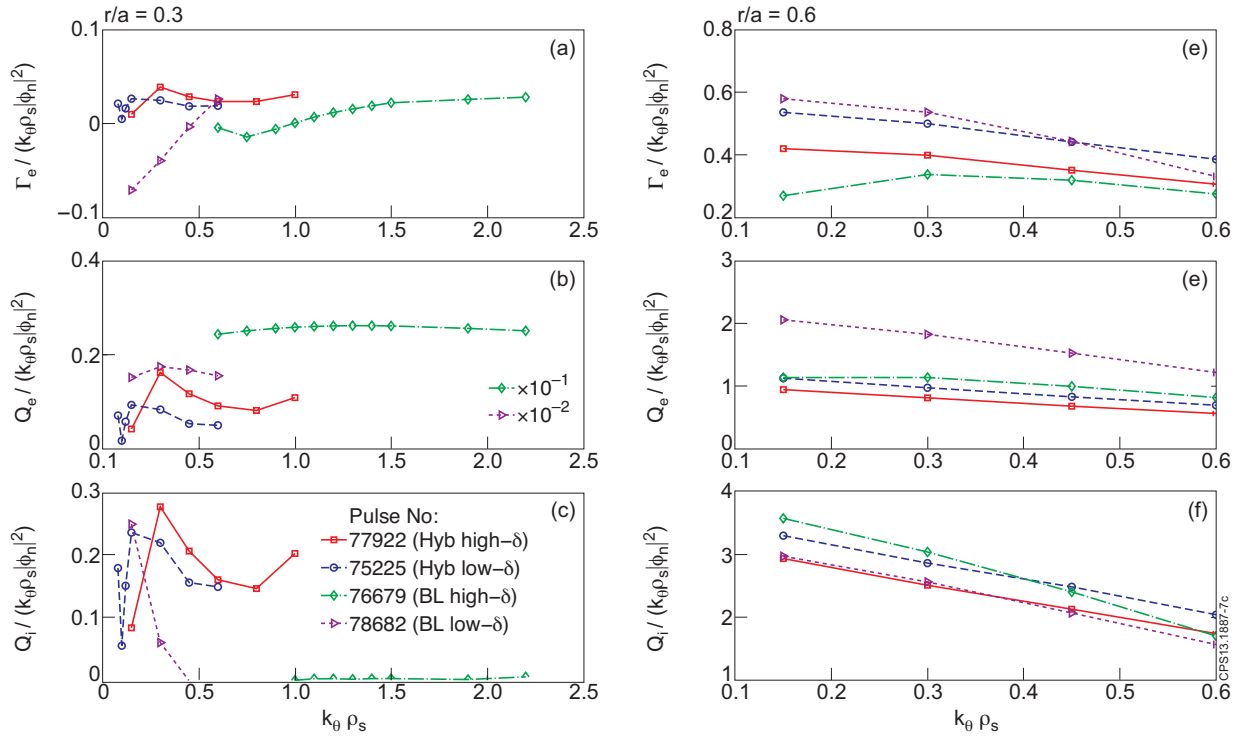

Figure 7: Normalized linear particle (a,d), and heat fluxes of electrons (b,e) and ions (c,f); left figures at r/a = 0.3, and right figures at r/a = 0.6. Solid (red) lines correspond to the values for Pulse No: 77922, dashed (blue) lines for Pulse No: 75225, dashed-dotted (green) lines for Pulse No: 76679, and dotted (mauve) lines for Pulse No: 78682 discharges.

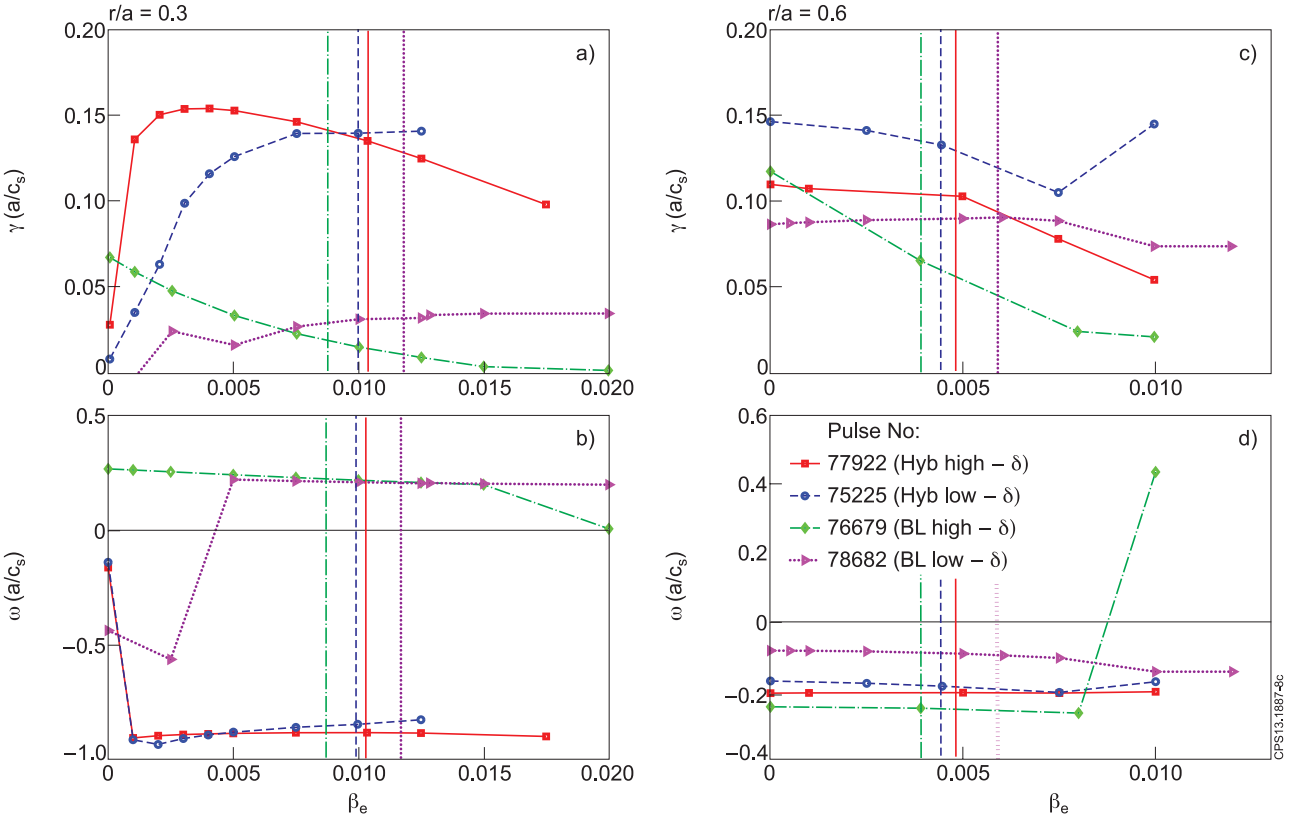

Figure 8: Imaginary and real frequency of the most linearly unstable modes as functions of β_e with self-consistent variation of the α_{MHD}; (a,b) at r/a = 0.3, and (c,d) at r/a = 0.6. Solid (red) lines correspond to the values for Pulse No: 77922, dashed (blue) lines for Pulse No: 75225, dashed-dotted (green) lines for Pulse No: 76679, and dotted (mauve) lines for Pulse No: 78682 discharges. The straight lines represent the experimental values for β_e colour coded similarly to the corresponding curves.

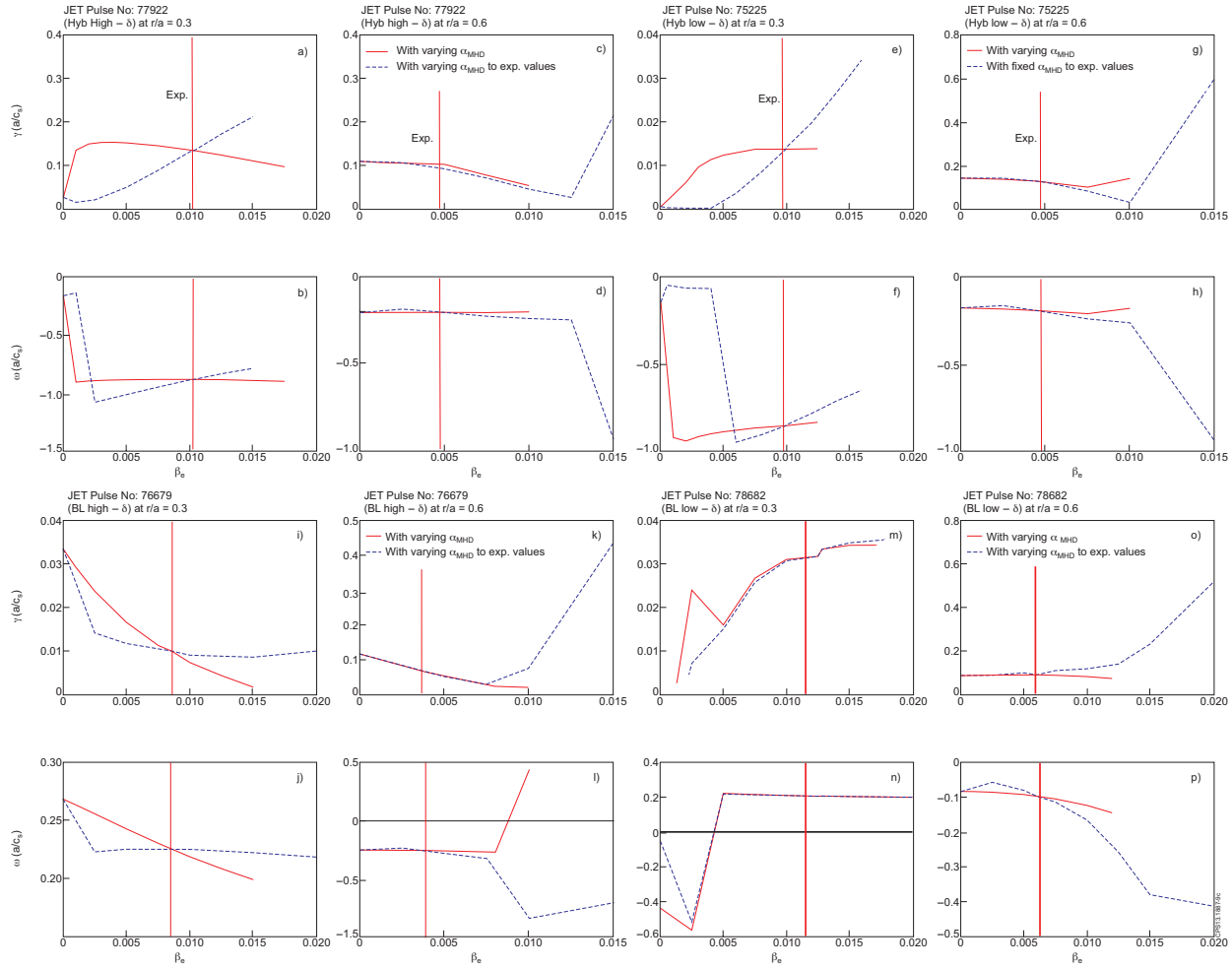

Figure 9: Imaginary and real frequency of the most unstable modes as functions of β_e with selfconsistent variation of the α_{MHD} solid (red) lines, and with fixed MHD dashed (blue) lines. (a,b) at r/a = 0.3 and (c,d) at r/a = 0.6 for Pulse No: 77922 discharge, (e,f) at r/a = 0.3 and (g,h) at r/a = 0:6 for Pulse No: 75225 discharge. (i,j) at r=a = 0.3 and (k,l) at r/a = 0.6 for Pulse No: 76679 discharge. (m,n) at r/a = 0.3 and (o,p) at r/a = 0.6 for Pulse No: 78682 discharge.

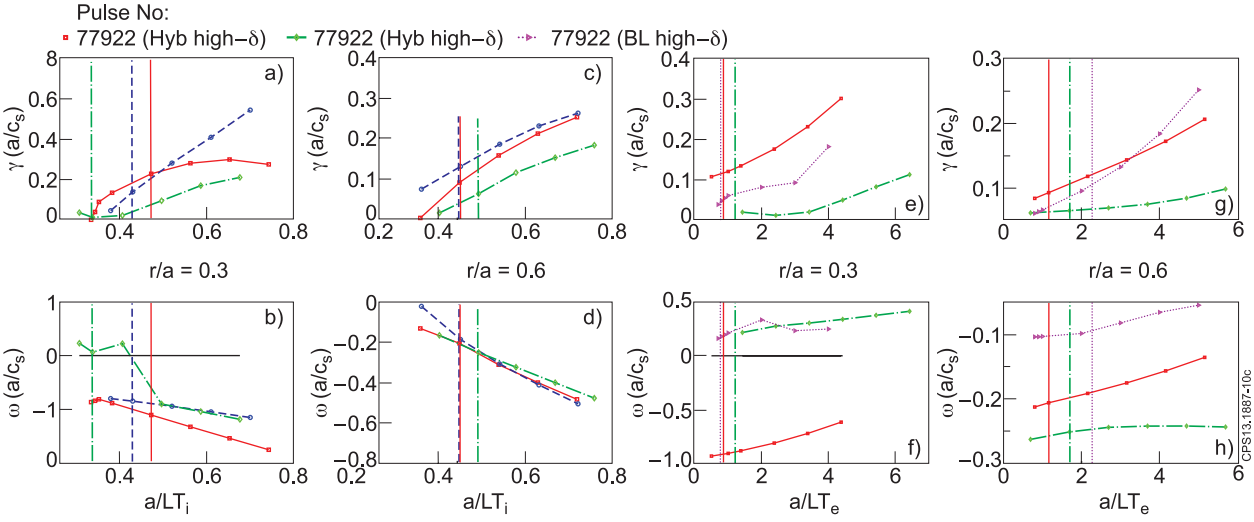

Figure 10: Imaginary and real frequency of the most linearly unstable modes as functions of a/LT_i (left), and a/LT_e (right). (a,b) and (e,f) at r/a = 0.3, (c,d) and (g,h) at r/a = 0.6. Solid (red) lines correspond to the values for Pulse No: 77922, dashed (blue) lines for Pulse No: 75225, dashed-dotted (green) lines for Pulse No: 76679, and dotted (mauve) lines for Pulse No: 78682 discharges. The straight lines represent the experimental values for $a/LT_{i,e}$ colour coded similarly to the corresponding curves.

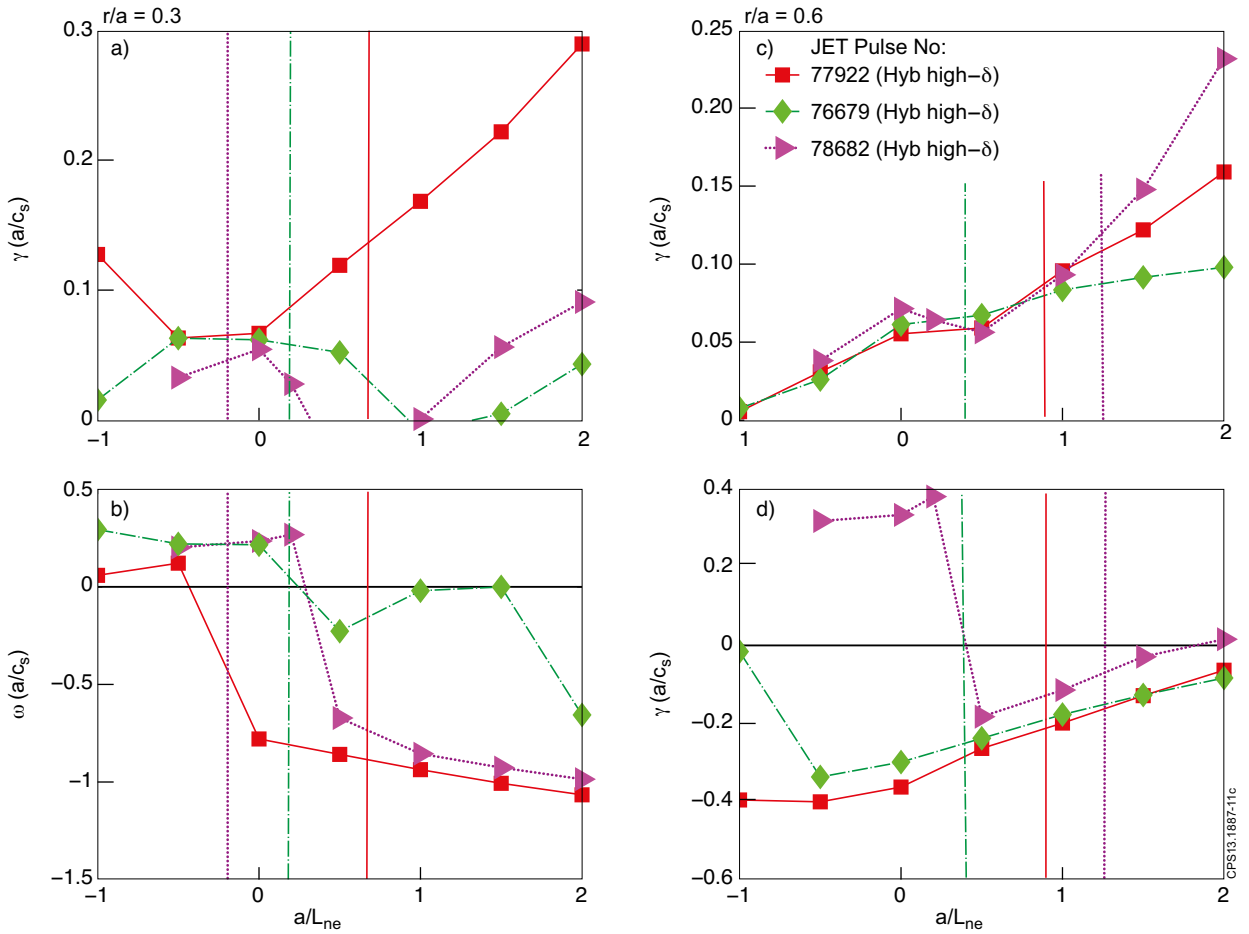

Figure 11: Imaginary and real frequency of the most linearly unstable modes as functions of a/Ln_e (right). (a,b) at r/a = 0.3, (c,d) at r/a = 0.6. Solid (red) lines correspond to the values for Pulse No: 77922, dashed-dotted (green) lines for Pulse No: 76679, and dotted (mauve) lines for Pulse No: 78682 discharges. The straight lines represent the experimental values for a/Ln_e colour coded similarly to the corresponding curves.

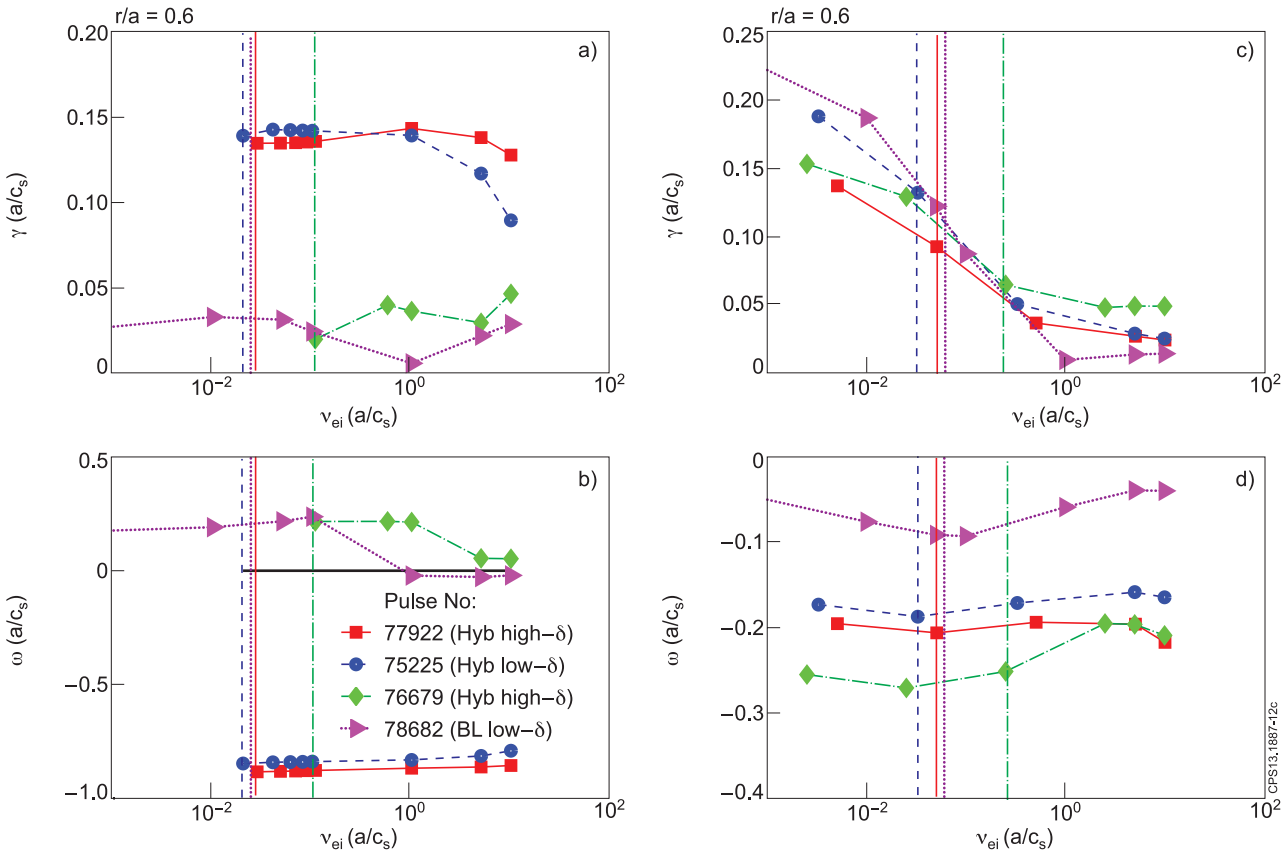

Figure 12: Imaginary and real frequency of the most linearly unstable modes as functions of $\nu_{ei}(a/c_s)$. (a,b) at r/a = 0.3, and (c,d) at r/a = 0.6. Solid (red) lines correspond to the values for Pulse No: 77922, dashed (blue) lines for Pulse No: 75225, dashed-dotted (green) lines for Pulse No: 76679, and dotted (mauve) lines for Pulse No: 78682. The straight lines represent the experimental values for $\nu_{ei}(a/c_s)$ colour coded similarly to the corresponding curves.

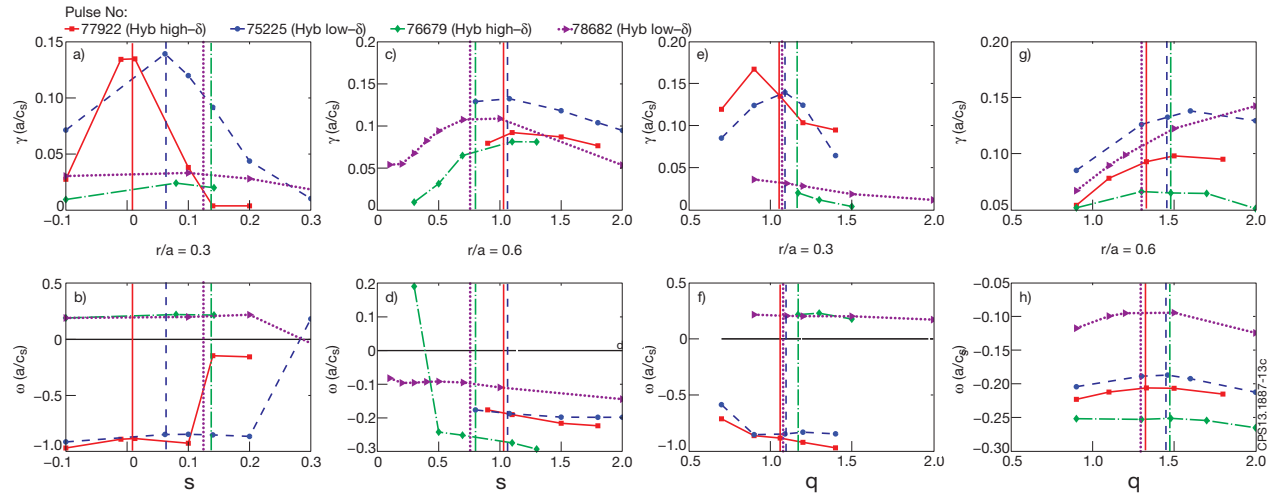

Figure 13: Imaginary and real frequency of the most linearly unstable modes as functions of s (left), and q (right). (a,b) and (e,f) at r/a = 0.3, (c,d) and (g,h) at r/a = 0.6. Solid (red) lines correspond to the values for Pulse No: 77922, dashed (blue) lines for 75225, dashed-dotted (green) lines for Pulse No: 76679, and dotted (mauve) lines for Pulse No: 78682. The straight lines represent the experimental values for s; q colour coded similarly to the corresponding curves.

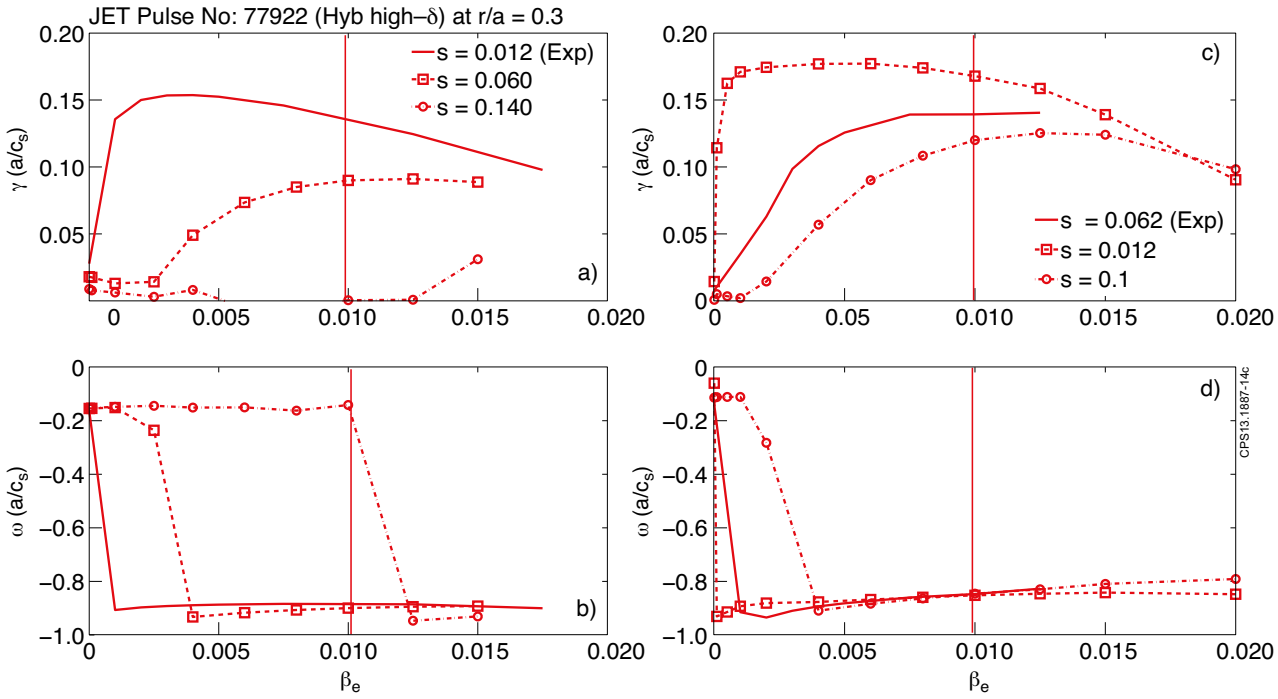

Figure 14: Imaginary and real frequency of the most linearly unstable modes at r/a = 0.3 as functions of β_e for various magnetic shear, s. (a,b) show the results for Pulse No: 77922, and (c,d) for Pulse No: 75225 JET discharges, where solid (red) lines correspond to the results obtained with experimental values of s. The straight lines represent the experimental values for β_e.

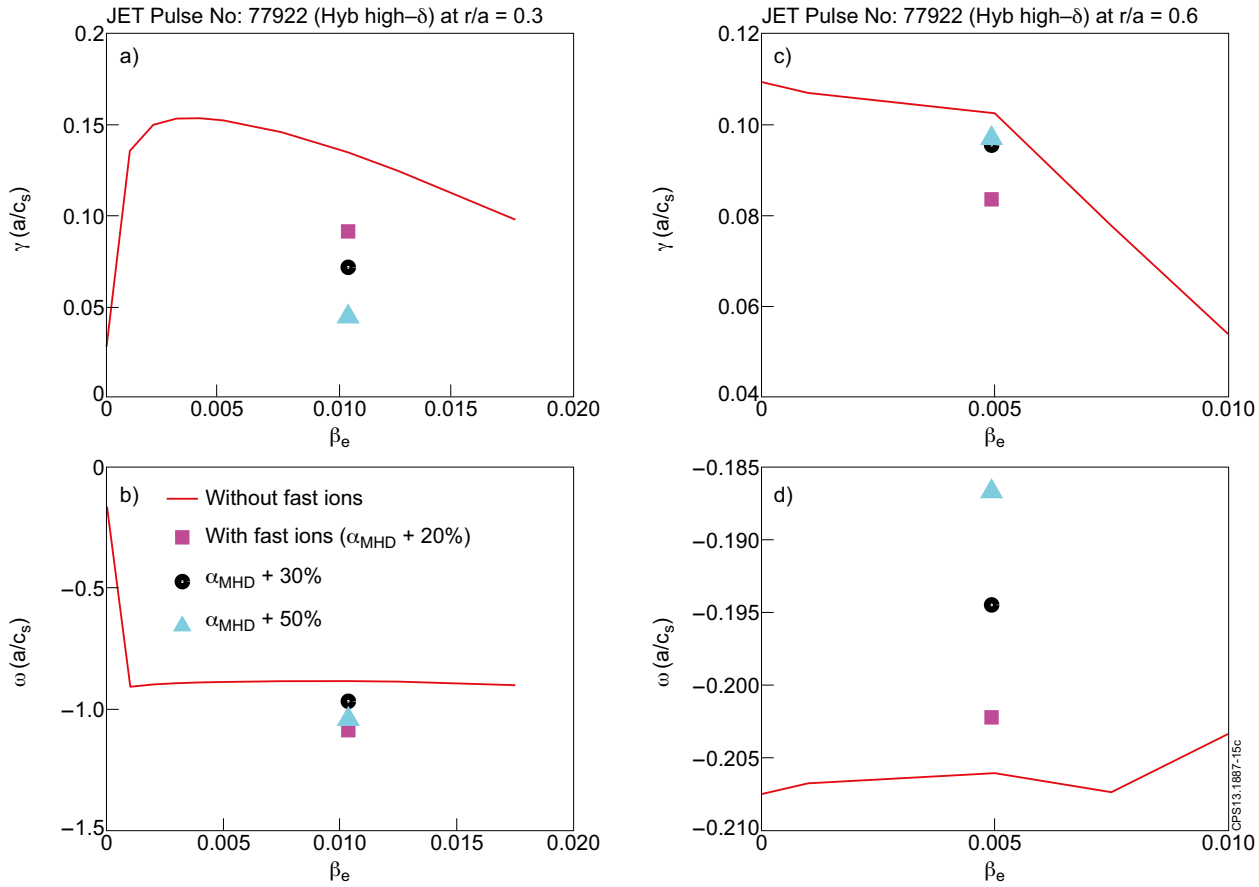

Figure 15: Imaginary and real frequency of the most unstable modes for JET Pulse No: 77922 as functions of β_e, where contributions from fast ions are included. (a,b) at r/a = 0.3 and (c,d) at r/a = 0.6. In this figure the red solid lines represent the results without the contribution from the fast ions, and square (mauve) symbols represent the results where the contribution from fast ions are considered. Further increase (artificially) of the impact of the fast ions on the α_{MHD} using the multiplier parameter c_p as defined in Eq.3, are shown with black circle (α_{MHD} + 30%) and blue triangle (α_{MHD} + 50%) symbols.

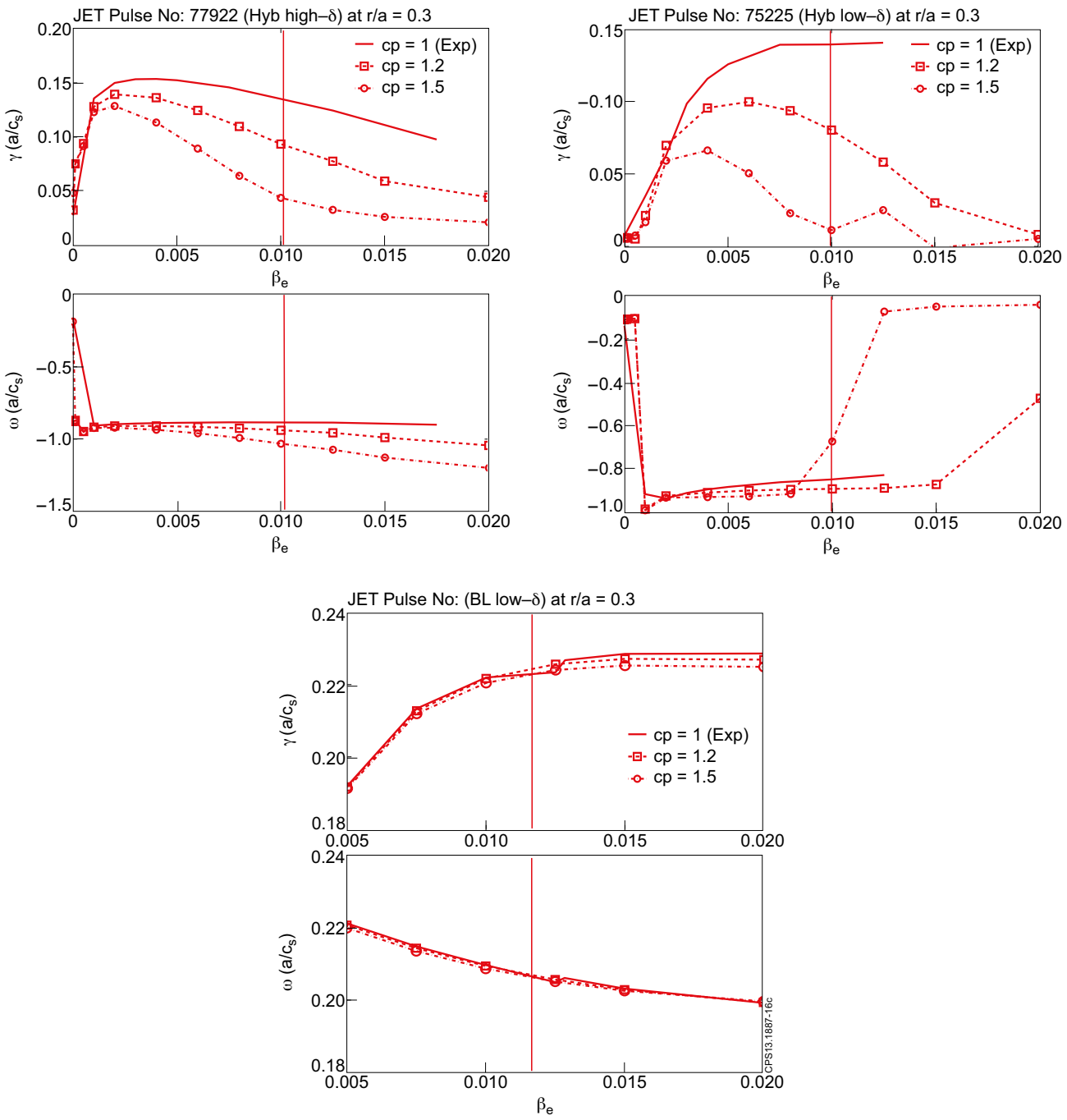

Figure 16: Imaginary and real frequency of the most linearly unstable modes at r/a = 0.3 as functions of β_e for various values of c_p. (a,b) show the results for Pulse No: 77922, (c,d) for Pulse No: 75225, and (e,f) for Pulse No: 78682 JET discharges, where solid (red) lines correspond to the results obtained with $c_p = 1$. The straight lines represent the experimental values for β_e.

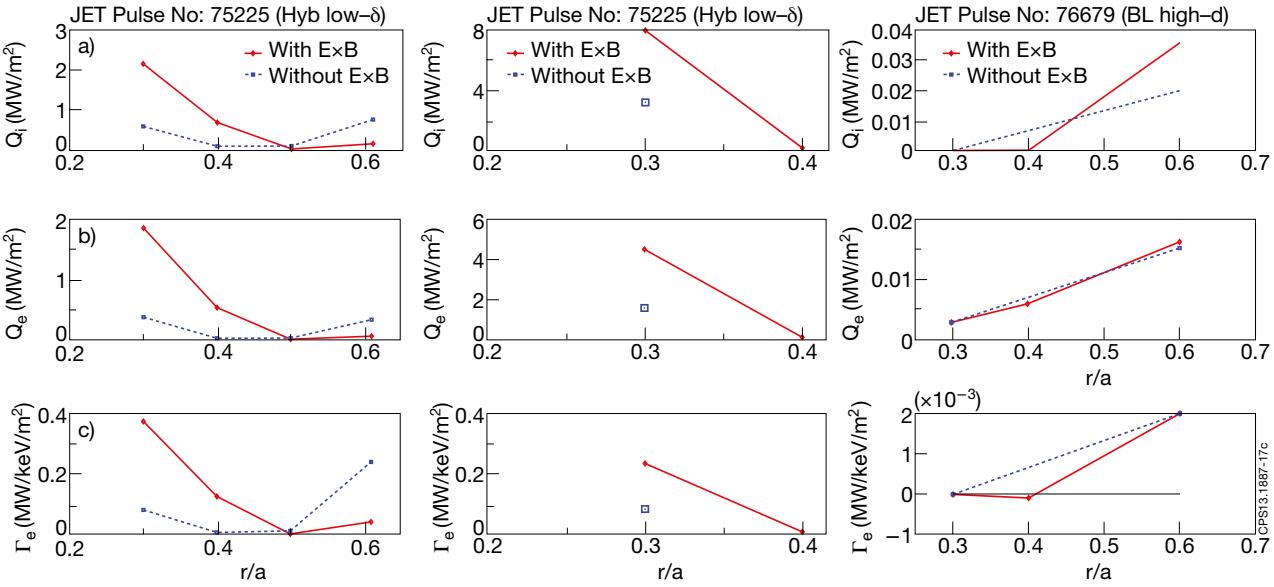

Figure 17: Non-linear heat fluxes of ion and electron, and particle flux of electrons versus r/a for the three selected JET Pulse No's: (a-c) 77922, (d-f) 75225, and (g-i) 76679. Solid (red) lines correspond to the results obtained with and dashed (blue lines) without ***E×B*** *shear effects.*